Mon. Not. R. Astron. Soc. **000**, 000–000 (2009) Printed 5 October 2009 (MN LaTeX style file v2.2)

arXiv:0906.4971v3 [astro-ph.CO] 5 Oct 2009

Kinematic deprojection and mass inversion of spherical systems of known velocity anisotropy

Gary A. Mamon[1,2]⋆ and Gwenaël Boué[1,3]†
[1] Institut d'Astrophysique de Paris (UMR 7095: CNRS & UPMC), 98 bis Bd Arago, F–75014 Paris, France
[2] Astrophysics & BIPAC, University of Oxford, Keble Rd, Oxford OX1 3RH, UK
[3] Astronomie et Systèmes Dynamiques, IMCCE-CNRS UMR8028, Observatoire de Paris, UPMC, 77 Av. Denfert-Rochereau, F-75014 Paris, France

Accepted 2009 October 2. Received 2009 October 1; in original form 2009 June 29

ABSTRACT
Traditionally, the degeneracy between the unknown radial profiles of total mass and velocity anisotropy inherent in the spherical, stationary, non-streaming Jeans equation has been handled by assuming a mass profile and fitting models to the observed kinematical data. However, mass profiles are still not well known: there are discrepancies in the inner slopes of the density profiles of halos found in dissipationless cosmological N-body simulations, and the inclusion of gas alters significantly the inner slopes of both the total mass and the dark matter component. Here, the opposite approach is considered: the equation of anisotropic kinematic projection is inverted for known arbitrary anisotropy to yield the space radial velocity dispersion profile in terms of an integral involving the radial profiles of anisotropy and isotropic dynamical pressure (itself a single integral of observable quantities). Then, through the Jeans equation, the mass profile of a spherical system is derived in terms of double integrals of observable quantities. Single integral formulas for both deprojection and mass inversion are provided for several simple anisotropy models (isotropic, radial, circular, general constant, Osipkov-Merritt, Mamon-Łokas and Diemand-Moore-Stadel). Tests of the mass inversion on NFW models with the first four of these anisotropy models yield accurate results in the case of perfect observational data, and typically better than 70% (in 4 cases out of 5) accurate mass profiles for the sampling errors expected from current observational data on clusters of galaxies. For the NFW model with mildly increasing radial anisotropy, the mass is found to be insensitive to the adopted anisotropy profile at 7 scale radii and to the adopted anisotropy radius at 3 scale radii. This anisotropic mass inversion method is a useful complementary tool to analyze the mass and anisotropy profiles of spherical systems. It provides the practical means to lift the mass-anisotropy degeneracy in quasi-spherical systems such as globular clusters, round dwarf spheroidal and elliptical galaxies, as well as groups and clusters of galaxies, when the anisotropy of the tracer is expected to be linearly related to the slope of its density (Hansen & Moore 2006).

Key words: stellar dynamics – dark matter – methods: analytical – galaxies: kinematics and dynamics – galaxies: haloes – galaxies: clusters, general

1 INTRODUCTION

The major goal of kinematical modelling of a self-gravitating astrophysical system, observed at one instant, is to measure on one hand the total mass distribution (visible and dark matter), and on the other hand the three dimensional velocity streaming and dispersion moments. In other words, the modeller wishes to deduce the distributions of dark matter and of orbital shapes. The modeller has at his disposal, at best, maps of surface density (or surface brightness) and of the velocity field at each point, or else its moments (line-of-sight mean velocity, dispersion, skewness and kurtosis).

The basic equation for such kinematical modelling is the *collisionless Boltzmann equation* (hereafter CBE, but also often called Liouville or Vlasov, see Hénon 1982), which states the incompressibility of the system in 6-dimensional phase (position,velocity) space:

$$\frac{\partial f}{\partial t} + \mathbf{v}\cdot\nabla f - \nabla\Phi\cdot\frac{\partial f}{\partial \mathbf{v}} = 0\ ,$$

⋆ E-mail: gam@iap.fr
† E-mail: boue@imcce.fr

© 2009 RAS

where Φ is the gravitational potential (hereafter potential) and f is the *distribution function*, that is the density in phase space. Unfortunately, the resolution of the CBE is difficult, especially when projection equations are taken into account.[1] In particular, the CBE presents a degeneracy between the unknown potential and the unknown velocity field (given that observations usually limit the velocities to their projection along the line-of-sight, measured through redshifts).

The traditional simpler approach has been to use the (first) velocity moments of the CBE, which are more easily related to observables, the *Jeans equations* that pertain to local dynamical equilibrium

$$\frac{\partial \overline{\mathbf{v}}}{\partial t} + (\overline{\mathbf{v}}\cdot\nabla)\overline{\mathbf{v}} = -\nabla\Phi - \frac{1}{\rho}\nabla\cdot\left(\rho\,\boldsymbol{\sigma^2}\right) \ , \tag{1}$$

where ρ is the space density of the *tracer* used to observe the system, $\boldsymbol{\sigma^2}$ is the tracer's dispersion tensor, whose elements are $\sigma^2_{ij} = \overline{v_i\,v_j} - \overline{v_i}\,\overline{v_j}$, and $\rho\,\boldsymbol{\sigma^2}$ is the *anisotropic dynamical pressure tensor* of the tracer. With the simplifying assumptions of stationarity and the absence of streaming motions, equation (1) simplifies to the *stationary non-streaming Jeans equations*:

$$\nabla\cdot\left(\rho\,\boldsymbol{\sigma^2}\right) = -\rho\,\nabla\Phi \ . \tag{2}$$

Using the stationary non-streaming Jeans equations (2), one can relate the orbital properties, contained in the pressure term with the mass distribution contained in the potential (through Poisson's equation).

The small departures from circular symmetry of many astrophysical systems observed in projection, such as globular clusters, the rounder elliptical galaxies (classes E0 to E2), and groups and clusters of galaxies, has encouraged dynamicists to assume spherical symmetry to perform the kinematical modelling. The *stationary non-streaming spherical Jeans equation* can then be simply written

$$\frac{\mathrm{d}\left(\rho\,\sigma_r^2\right)}{\mathrm{d}r} + 2\,\frac{\beta}{r}\,\rho\,\sigma_r^2 = -\rho(r)\,\frac{GM(r)}{r^2} \ , \tag{3}$$

where $M(r)$ is the *total* mass profile, while

$$\beta(r) = 1 - \frac{\sigma_\theta^2+\sigma_\phi^2}{2\,\sigma_r^2} = 1 - \frac{\sigma_\theta^2}{\sigma_r^2} \ ,$$

is the tracer's *velocity anisotropy* (hereafter, *anisotropy*) profile, with $\sigma_r \equiv \sigma_{rr}$, etc., $\sigma_\theta = \sigma_\phi$, by spherical symmetry, and with $\beta = 1$, 0, $\to -\infty$ for radial, isotropic and circular orbits, respectively. The stationary non-streaming spherical Jeans equation provides an excellent estimate of the mass profile, given all other 3D quantities, in slowly-evolving triaxial systems such as halos in dissipationless cosmological simulations (Tormen, Bouchet, & White 1997) and elliptical galaxies formed by mergers of gas-rich spirals in dissipative N-body simulations (Mamon et al. 2006).

Again, one is left with having two unknown quantities, the radial profiles of mass and velocity anisotropy, linked by a single equation. In other words, we have to deal with a serious *mass-anisotropy degeneracy*.

The simplest and most popular approach is to assume parametric forms for both the mass and anisotropy profiles. One can then express the product of the observable quantities: *surface density* profile $\Sigma(R)$ and *line of sight square velocity dispersion* profile $\sigma^2_{\rm los}(R)$ vs. *projected radius* R through the *anisotropic kinematic projection equation* (Binney & Mamon 1982) expressing the *projected dynamical pressure* $P = \Sigma\sigma^2_{\rm los}$:

$$\begin{aligned} P(R) = \Sigma(R)\,\sigma^2_{\rm los}(R) &= 2\int_R^\infty \left[\left(r^2-R^2\right)\,\sigma_r^2 + R^2\sigma_\theta^2\right]\,\rho\,\frac{\mathrm{d}r}{r\sqrt{r^2-R^2}} && (4)\\ &= 2\int_R^\infty \left(1-\beta\,\frac{R^2}{r^2}\right)\,p\,\frac{r\,\mathrm{d}r}{\sqrt{r^2-R^2}} \ , && (5)\end{aligned}$$

where equation (5) is only valid for non-circular orbits, and where $p = \rho\sigma_r^2$ is the *radial dynamical pressure*.

Inserting the radial pressure[2] (eq. [5]) in the spherical stationary Jeans equation (3), one determines the line of sight velocity dispersions essentially through a double integration over $\rho\,M\,\mathrm{d}r$. Mamon & Łokas (2005b, Appendix) have simplified the problem by writing the projected pressure as a single integral

$$P(R) = \Sigma(R)\,\sigma^2_{\rm los}(R) = 2\,G\int_R^\infty K_{\rm proj}[r,R|\beta(r)]\,\rho\,M\,\frac{\mathrm{d}r}{r} = 2\int_R^\infty K_{\rm proj}[r,R|\beta(r)]\,\rho\,v_c^2\,\mathrm{d}r \ , \tag{6}$$

where they were able to determine simple analytical expressions for the dimensionless kernel $K_{\rm proj}$ for several popular analytical formulations of $\beta(r)$. Note that if one assumes isotropy, the equations are greatly simplified, and one finds (Tremaine et al. 1994; Prugniel & Simien 1997) $K_{\rm proj}(r,R) = \sqrt{1-R^2/r^2}$. Also, if $\beta = \mathrm{cst} \neq 0$, the kernel can be expressed either in terms of incomplete Beta functions (Mamon & Łokas 2005b), or in terms of the easier to compute regularized incomplete Beta functions (Mamon & Łokas 2006). With parametric choices of the mass profile $M(r)$ and anisotropy profile $\beta(r)$, one can fit for the free parameters of these two profiles that lead to the best match of the observed line of sight velocity dispersion profile. The drawback of this *indirect method*, even with the recent introduction of these simplifying kernels, is that the analysis is *doubly-parametric*, so that the derived parameters will be meaningless if one does not choose the correct form for both the mass and anisotropy profiles.

---

[1] Note that for *dynamical* studies, a fast computer code has been recently developed by Alard & Colombi (2005) that solves the CBE in 1+1 dimensions, and a 3+3 dimension code is under development by G. Lavaux and these authors.

[2] For clarity, we hereafter drop the term *dynamical* before *pressure*.

The next step in complexity is to perform a *single-parametric* analysis: either isotropy is assumed to *directly* obtain the mass profile, which we call the *mass inversion*, which is the focus of the present paper. Alternatively, a mass profile can be assumed and *one directly* determines the anisotropy profile through the *anisotropy inversion*, first derived by Binney & Mamon (1982), with later and progressively simpler solutions found by Tonry (1983), Bicknell et al. (1989), Solanes & Salvador-Solé (1990), and Dejonghe & Merritt (1992). One can attempt to lift the mass-anisotropy degeneracy by considering together the variation with projected radius of the line-of-sight velocity dispersion *and kurtosis* (Łokas 2002; Łokas & Mamon 2003). For halos in cosmological simulations, which are not far from spherical (Jing & Suto 2002 and references therein) and nearly isotropic (Mamon & Łokas 2005b and references therein), viewed in projection, this dispersion-kurtosis analysis yields fairly accurate masses, concentrations and anisotropies (Sanchis, Łokas, & Mamon 2004). Unfortunately, the line-of-sight projection of the 4th order Jeans equation, required in the dispersion-kurtosis method, is only possible when $\beta = \mathrm{cst}$, which does not appear to be realistic for elliptical galaxies formed by major mergers (Dekel et al. 2005).

An even more sophisticated and general approach is to adopt a potential and minimize the residuals between the predicted and true observables, i.e. the distribution of objects in projected phase space $(R, v_{\rm los})$ (where $v_{\rm los}$ is the line of sight velocity) by one of several methods involving the distribution function:

(i) A general global form for the distribution function is adopted, in terms of known integrals of motions. For example, in spherical systems with isotropic non-streaming velocities, the distribution function is a function of energy only, while in anisotropic non-streaming spherical systems it is a function of energy and the modulus of the angular momentum. Alas, there is no known realistic form for $f = f(E, \mathbf{J})$ for anisotropic non-streaming spherical systems nor for non-spherical systems, although Wojtak et al. (2008) have recently shown that cosmological halos have distribution functions that can be written $f(E,J) = f_E(E)\, J^{2\,(\beta_\infty-\beta_0)} \left(1+J^2/J_0^2\right)^{-\beta_0}$, where we adopt hereafter the notations $\beta_0 = \beta(0)$ and $\beta_\infty = \lim_{r\to\infty} \beta$, where J_0 is a free parameter related to the 'anisotropy' radius where $\beta(r) = (\beta_0+\beta_\infty)/2$. Unfortunately, Wojtak et al. do not provide an analytical formula for $f_E(E)$.

(ii) A set of elementary distribution functions of E or (E, J) is chosen, as first proposed by Dejonghe (1989), then Merritt & Saha (1993), and applied to elliptical galaxies by Gerhard et al. (1998). One then searches the linear combination of these distribution functions, with positive weights (to ensure a positive global distribution function) that minimizes the residuals between the predicted and true observables. However, there is no guarantee that the set of elementary distribution functions constitute a basis set, so that some global realistic distribution functions may be missed. Moreover, the distribution function may depend on an additional unknown integral of motion.

(iii) A set of delta- distribution functions, $f = f(E, \mathbf{J})$ is chosen, in other words one considers orbits of given E and $\mathbf{J}$ (Schwarzschild 1979; Richstone & Tremaine 1984; Syer & Tremaine 1996). Again one searches for a linear combination of these orbits that minimises the residuals between predicted and true observables, again enforcing positive weights. These weights are obtained either by averaging the observables over an orbit (Schwarzschild) or by continuously updating them (Syer & Tremaine; de Lorenzi et al. 2007). This method is powerful enough to handle non-spherical potentials. Despite concerns about convergence (Cretton & Emsellem 2004; Valluri et al. 2004), the orbit-superposition method, if properly implemented, does reproduce the correct solutions (Richstone et al. 2004; Thomas et al. 2004).

The potential can be adapted from the observations, assuming constant mass-to-light ratio (M/L) if the observed density is a surface brightness, or constant mass-to-number ratio (M/N) if the observed density is a surface number density. If spherical symmetry is assumed, this involves a choice of M/L or M/N, the deprojection of the surface density map, and then Poisson's equation is easily inverted to obtain the potential from the density. For axisymmetric systems, one can deproject the surface density maps into a potential assuming it to be the sum of gaussians (Emsellem, Monnet, & Bacon 1994). One can add to the potential a possible dark component given in parametric form (see, e.g., Williams et al. 2009).

Alternatively, instead of using distribution functions, one can fit the distribution of objects in projected phase space by the multiple parametric adjustment of the mass and anisotropy profiles, as well as possibly the velocity distribution in space (which could be non-gaussian, see Kazantzidis et al. 2004; Wojtak et al. 2005; Hansen et al. 2006), as in the MAMPOSSt method (Mamon, Biviano & Boué, in preparation).

Returning to direct single-parametric estimations, the mass profile of astronomical systems does not seem to be better established than the anisotropy profile. Indeed, despite early claims (Navarro, Frenk, & White 1996, hereafter NFW) of a universal density profile for the structures (*halos*) in dissipationless cosmological N-body simulations of a flat Universe of cold dark matter with a cosmological constant (hereafter ΛCDM), there has been an ongoing debate on whether the inner slope is steeper (Fukushige & Makino 1997; Moore et al. 1999) or shallower (Navarro et al. 2004; Stoehr et al. 2002; Stoehr 2006). Furthermore, the inclusion of gas in cosmological simulations can lead to much steeper dark matter density profiles (Gnedin et al. 2004). Indeed, the dissipative nature of baryons leads them to accumulate in the centers of systems, not only in spiral galaxies, as is well known, but also in elliptical galaxies, for otherwise the NFW-like mass distribution as found in ΛCDM halos would lead to a local M/L and aperture velocity dispersion much lower than observed (Mamon & Łokas 2005a), and the dominance of baryons in the center and dark matter in the envelopes has been recently confirmed by X-ray measurements (Humphrey et al. 2006). Moreover, the dark matter dynamically responds to the baryons that dominate in the inner regions, to reach steeper slopes than they would have had without the presence of baryons (Blumenthal et al. 1986; Gnedin et al. 2004). But the final density profile of dark matter is expected to be very sensitive to the details of the baryonic feedback processes.

On the other hand, the anisotropy profiles of the halos in dissipationless cosmological simulations appears to be fairly universal (see the compilation by Mamon & Łokas 2005b and references therein, and Wojtak et al. 2008), although galaxy-mass halos have somewhat more radial orbits than cluster-sized halos (Ascasibar & Gottlöber 2008). Also a similar shape of anisotropy profile holds in N-body+SPH simulations of merging spirals galaxies, including gas, but with a ratio of anisotropy to virial radius that is ten times smaller (Dekel et al. 2005). Moreover, dissipationless N-body simulations (cosmological and binary mergers) indicate that the anisotropy is linearly related to the slope of the density profile (Hansen & Moore 2006), although the trend is less clear in elliptical galaxies formed in N-body+SPH simulations as merger remnants of spiral galaxies (Mamon et al. 2006), because of the dynamical interaction of the stellar, dark matter and dissipative gas components.

In this paper, we derive and test the mathematics of the mass inversion. We begin in Sect. 2.1 with a reminder on the kinematic deprojection of isotropic systems, followed by the mass inversion of isotropic systems in Sect. 2.2. We then develop in Sect. 2.3 our algorithm for the kinematic deprojection of anisotropic systems, and in Sect. 2.4 we deduce the mass profile with the Jeans equation (3). In Sect. 3, we test our mass inversion methods.

The reader in a hurry might want to skip the mathematical details. (S)he will find the general anisotropic deprojection formulae in equation (32), with special cases given in equations (39) [radial orbits], (44) [circular orbits], and in equations (62) [constant $\beta < 1$, Osipkov-Merritt, Mamon-Łokas, and Diemand-Moore-Stadel], with C_β given in Table 2 and kernels $K_{\rm i}$ given in equations (37) [constant $\beta < 1$], (48) [Osipkov-Merritt], (53) [Mamon-Łokas], and (61) [Diemand-Moore-Stadel]. The formulae for the mass inversion will be found in equations (69) [general], (74) [radial], (76) [circular], and (83) [constant $\beta < 1$, Osipkov-Merritt, Mamon-Łokas, and Diemand-Moore-Stadel] with the same C_β and kernels, and with D_β also given in Table 2.

In the very late stages of this work, we came across a draft of Wolf et al. (2009), who independently developed an analogous method for anisotropic kinematic deprojection. While Wolf et al. produce a general formula for kinematic deprojection, the present article also provides simpler formulae for the kinematic deprojection with specific simple anisotropy profiles, as well as general and specific formulae for the mass profile.

2 METHOD

2.1 Kinematic deprojection of isotropic systems

We begin by reviewing the mathematical formalism for the kinematic deprojection of isotropic systems. The *structural projection equation*, relating the space density $\rho(r)$ to the (projected) surface density $\Sigma(R)$:

$$\Sigma(R) = \int_{-\infty}^{\infty} \rho(r)\,{\rm d}z = 2\int_R^\infty \frac{\rho(r)\,r\,{\rm d}r}{(r^2-R^2)^{1/2}} \ , \tag{7}$$

is inverted through the usual Abel transform, whose derivation we recall in appendix A, as we will use it in the following subsection. One then recovers the well-known *structural deprojection* or *Abel inversion* equation

$$\rho(r) = -\frac{1}{\pi}\int_r^\infty \frac{{\rm d}\Sigma}{{\rm d}R}\,\frac{{\rm d}R}{(R^2-r^2)^{1/2}} \ . \tag{8}$$

In the case of isotropic velocities one can express the projected dynamical pressure $\Sigma\,\sigma_{\rm los}^2$ in terms of the dynamical pressure $\rho\,\sigma^2$ with the *isotropic kinematical projection equation*, obtained by setting $\beta = 0$ in the anisotropic kinematic projection equation (5):

$$\Sigma\,\sigma_{\rm los}^2 = 2\int_R^\infty \rho\,\sigma^2\,\frac{r\,{\rm d}r}{\sqrt{r^2-R^2}} \ . \tag{9}$$

Equation (9) is the strict analog to equation (7), where the tracer densityρ is replaced by the dynamical pressure $p = \rho\,\sigma^2$ and the surface density Σ is replaced by projected pressure $P = \Sigma\,\sigma_{\rm los}^2$.[3] With these replacements, the structural deprojection equation (8) turns into the *isotropic kinematical deprojection equation*

$$p_{\rm iso}(r) \equiv \left[\rho(r)\,\sigma^2(r)\right]_{\beta=0} = -\frac{1}{\pi}\int_r^\infty \frac{{\rm d}P}{{\rm d}R}\,\frac{{\rm d}R}{\sqrt{R^2-r^2}} \ . \tag{10}$$

2.2 Mass inversion of isotropic systems

Now, from the stationary non-streaming spherical Jeans equation (3), with the isotropic condition ($\beta = 0$), the total mass profile is trivially

$$M(r) = -\frac{r^2}{G\,\rho}\,\frac{{\rm d}p_{\rm iso}}{{\rm d}r} = \frac{1}{\pi}\,\frac{r^2}{G\,\rho}\,\frac{\rm d}{{\rm d}r}\int_r^\infty \frac{{\rm d}P}{{\rm d}R}\,\frac{{\rm d}R}{\sqrt{R^2-r^2}} \ . \tag{11}$$

With the variable substitution $R = r\,u$, we can avoid the singularity in the surface term of the derivative of the integral of equation (10) or (11) by writing

$$p'_{\rm iso}(r) \equiv \frac{{\rm d}p_{\rm iso}}{{\rm d}r} = -\frac{1}{\pi}\,\frac{\rm d}{{\rm d}r}\int_r^\infty \frac{{\rm d}P}{{\rm d}R}\,\frac{{\rm d}R}{\sqrt{R^2-r^2}} = -\frac{1}{\pi}\int_1^\infty P''(ru)\frac{u\,{\rm d}u}{\sqrt{u^2-1}} = -\frac{1}{\pi\,r}\int_r^\infty \frac{{\rm d}^2P}{{\rm d}R^2}\,\frac{R\,{\rm d}R}{\sqrt{R^2-r^2}} \ , \tag{12}$$

where $P''(R) = {\rm d}^2P/{\rm d}R^2$. Inserting the right-hand-side of equation (12) into the first equality of equation (11), we then obtain the *isotropic mass inversion equation*

$$M(r) = -\frac{r}{G}\,\frac{\displaystyle\int_r^\infty \frac{{\rm d}^2\left(\Sigma\sigma_{\rm los}^2\right)}{{\rm d}R^2}\,\frac{R\,{\rm d}R}{\sqrt{R^2-r^2}}}{\displaystyle\int_r^\infty \frac{{\rm d}\Sigma}{{\rm d}R}\,\frac{{\rm d}R}{\sqrt{R^2-r^2}}} \ , \tag{13}$$

---

[3] Given the isotropy, the space velocity dispersion is equal to the radial velocity dispersion, so we drop the subscript 'r'.

Table 1. Nomenclature

Definition	full expression	abbreviated expression
space radius		r
projected radius		R
projected pressure	$\Sigma\,\sigma_{\rm los}^2$	P
radial pressure	$\rho\,\sigma_r^2$	p
tangential pressure	$\rho\,\sigma_\theta^2$	$p_\theta = (1-\beta)\,p$
anisotropy	$1-\sigma_\theta^2/\sigma_r^2$	β
circular velocity	$\sqrt{GM(r)/r}$	v_c

where we used the structural deprojection equation (8) to replace the density in the denominator. The isotropic mass inversion equation can be further simplified, expressing the *circular velocity*, $v_c^2 = GM/r$ as[4]

$$v_c^2(r) = \frac{1}{\pi\rho(r)} \int_r^\infty \frac{{\rm d}^2 P}{{\rm d}R^2}\, \frac{R\,{\rm d}R}{\sqrt{R^2-r^2}}\ . \tag{14}$$

Unfortunately, the mass and circular velocity profiles require the second derivative of the (observable) projected pressure $P = \Sigma\sigma_{\rm los}^2(R)$. The singularity $\left(R^2-r^2\right)^{-1/2}$ in the numerators of equations (13) and (14) prevents one from expressing the mass profile with single integrals derivatives of the projected dynamical pressure after a suitable integration by parts.

2.3 Kinematic deprojection of systems of arbitrary known anisotropy profile

2.3.1 General anisotropy

The anisotropic kinematic projection equation (5) is strictly valid for non-circular orbits (finite β). For circular orbits ($\sigma_r = 0$) equation (4) yields

$$P(R) = 2\,R^2 \int_R^\infty p_\theta \frac{{\rm d}r}{r\,\sqrt{r^2-R^2}}\ , \tag{15}$$

where

$$p_\theta = (1-\beta)\,p = \rho\,\sigma_\theta^2$$

is the *tangential dynamical pressure*. To guide the reader, Table 1 reviews the nomenclature adopted in this paper.

We repeat the steps of the standard (isotropic) Abel inversion (Appendix A), now defining

$$J(r) = \int_r^\infty P\, \frac{R\,{\rm d}R}{\sqrt{R^2-r^2}} \tag{16}$$

$$= -\int_r^\infty \frac{{\rm d}P}{{\rm d}R}\, \sqrt{R^2-r^2}\,{\rm d}R\ , \tag{17}$$

where equation (17) is obtained by integration by parts (the surface term is 0 for $P(R) \propto R^{-\alpha}$ with $\alpha > 1$).

For non-circular orbits, inserting the projected pressure (eq. [5]) into the definition of J (eq. [16]), one finds

$$J(r) = 2\int_r^\infty \frac{R\,{\rm d}R}{\sqrt{R^2-r^2}} \int_R^\infty \left(1-\beta\,\frac{R^2}{s^2}\right) p\, \frac{s\,{\rm d}s}{\sqrt{s^2-R^2}}\ , \tag{18}$$

$$= 2\int_r^\infty p\,s\,{\rm d}s \int_r^s \frac{R\,{\rm d}R}{\sqrt{(R^2-r^2)\,(s^2-R^2)}} - 2\int_r^\infty \beta\,p\,\frac{{\rm d}s}{s} \int_r^s \frac{R^3\,{\rm d}R}{\sqrt{(R^2-r^2)\,(s^2-R^2)}}\ , \tag{19}$$

$$= \frac{\pi}{2} \int_r^\infty \left[2 - \left(\frac{r^2}{s^2}+1\right)\beta\right] p\,s\,{\rm d}s\ , \tag{20}$$

where equation (19) is obtained after reversing the order of integration and the two inner integrals of eq. (19) are worth $\pi/2$ and $(\pi/4)(r^2+s^2)$, respectively. Differentiating equation (20), one has

$$\frac{{\rm d}J}{{\rm d}r} = -\pi\,r\,\left[(1-\beta)\,p + \int_r^\infty \beta\,p\,\frac{{\rm d}s}{s}\right]\ . \tag{21}$$

---

[4] We've never encountered in the literature the mass profile written in this direct fashion, although Romanowsky et al. (2009) gave the equivalent expression

$$v_c^2(r) = \frac{r^2}{\pi\rho(r)} \int_r^\infty \frac{{\rm d}(P'/R)}{{\rm d}R}\, \frac{{\rm d}R}{\sqrt{R^2-r^2}}\ .$$

The expression in equation (14) seems preferable as the differentiation is performed in a single pass.

Now, equation (17) can be differentiated to yield

$$\frac{\mathrm{d}J}{\mathrm{dr}} = r \int_r^\infty \frac{\mathrm{d}P}{\mathrm{d}R}\,\frac{\mathrm{d}R}{\sqrt{R^2-r^2}} = -\pi\, r\, p_{\rm iso}(r)\ , \tag{22}$$

where the second equality in equation (22) comes from equation (10). Equations (21) and (22) yield

$$p_\theta(r) = p_{\rm iso}(r) - \int_r^\infty \beta\, p\, \frac{\mathrm{d}s}{s}\ . \tag{23}$$

Equation (23) is an implicit integral equation for p with $p_{\rm iso}$ (eq. [10]) and β known. For finite $\beta < 1$, we solve for p by differentiating equation (23), to get the differential equation

$$p' - \frac{r\,\beta' + \beta}{1-\beta}\,\frac{p}{r} = \frac{p'_{\rm iso}}{1-\beta}\ . \tag{24}$$

Now, if we write

$$p' - \frac{r\,\beta' + \beta}{1-\beta}\,\frac{p}{r} = \frac{1}{g}\,\frac{\mathrm{d}(g\,p)}{\mathrm{d}r}\ , \tag{25}$$

then equations (24) and (25) lead to

$$p(r) = -\frac{1}{g(r)} \int_r^\infty \frac{g\,p'_{\rm iso}}{1-\beta}\,\mathrm{d}s\ , \tag{26}$$

where the upper limit at infinity ensures that the radial pressure $p = \rho\,\sigma_r^2$ does not reach negative values at a finite radial distance. But equation (25) directly gives

$$\frac{\mathrm{d}\ln f}{\mathrm{d}\ln r} = -\frac{-r\,\beta' + \beta}{1-\beta}\ ,$$

hence

$$g(r) = g(r_1)\, \exp\left(-\int_{r_1}^r \frac{s\,\beta' + \beta}{1-\beta}\,\frac{\mathrm{d}s}{s}\right) \tag{27}$$

for any arbitrary r_1. With equation (27), equation (26) leads to

$$\begin{aligned} p(r) &= -\exp\left(\int_{r_1}^r \frac{s\,\beta'+\beta}{1-\beta}\,\frac{\mathrm{d}s}{s}\right) \int_r^\infty \exp\left(-\int_{r_1}^s \frac{t\,\beta'+\beta}{1-\beta}\,\frac{\mathrm{d}t}{t}\right) \frac{p'_{\rm iso}}{1-\beta}\,\mathrm{d}s\ , \\ &= -\int_r^\infty \exp\left(-\int_r^s \frac{t\,\beta'+\beta}{1-\beta}\,\frac{\mathrm{d}t}{t}\right) \frac{p'_{\rm iso}}{1-\beta}\,\mathrm{d}s\ , \end{aligned} \tag{28}$$

where the second equality is obtained adopting $r_1 = r$.

One wishes to avoid the second derivative of the observables that occurs in the expression of equation (12) for $p'_{\rm iso}(r)$, which will amplify any uncertainties on the measurements of these observables. Integrating by parts the integral in equation (28), we finally obtain

$$p(r) = \frac{p_{\rm iso}(r)}{1-\beta(r)} - \int_r^\infty p_{\rm iso}(s)\,\frac{A_\beta(r,s)}{1-\beta(s)}\,\frac{\mathrm{d}s}{s}\ , \tag{29}$$

where $p_{\rm iso}$ is given in equation (10), and where

$$A_\beta(r,s) = \frac{\beta(s)}{1-\beta(s)}\, \exp\left(-\int_r^s \frac{t\,\beta'+\beta}{1-\beta}\,\frac{\mathrm{d}t}{t}\right)\ , \tag{30}$$

which is provided in Table 2 for various simple anisotropy models.

One may prefer to use the tangential dynamical pressure instead of the radial one, as it can be expressed in a slightly simpler form:

$$\begin{aligned} p_\theta(r) &= -\int_r^\infty \exp\left(-\int_r^s \frac{\beta}{1-\beta}\,\frac{\mathrm{d}t}{t}\right) p'_{\rm iso}\,\mathrm{d}s\ , \qquad (31) \\ &= p_{\rm iso}(r) - \int_r^\infty p_{\rm iso}\frac{\beta}{1-\beta}\, \exp\left(-\int_r^s \frac{\beta}{1-\beta}\,\frac{\mathrm{d}t}{t}\right)\frac{\mathrm{d}s}{s}\ , \\ &= p_{\rm iso}(r) - \int_r^\infty p_{\rm iso}(s)\, B_\beta(r,s)\,\frac{\mathrm{d}s}{s}\ , \qquad (32) \end{aligned}$$

as similarly derived in Appendix B, and where

$$B_\beta(r,s) = \frac{\beta(s)}{1-\beta(s)}\, \exp\left(-\int_r^s \frac{\beta}{1-\beta}\,\frac{\mathrm{d}t}{t}\right)\ , \tag{33}$$

Table 2. Terms in equations (34), (62) and (67) for specific anisotropy profiles

Anisotropy model	$A_\beta(r,s)$ (eq. [30])	$B_\beta(r,s)$ (eq. [33])	$C_\beta(r)$ (eq. [62])	$D_\beta(r)$ (eq. [67])
$\beta = \mathrm{cst}$	$\frac{\beta}{1-\beta}\left(\frac{r}{s}\right)^{\beta/(1-\beta)}$	$\frac{\beta}{1-\beta}\left(\frac{r}{s}\right)^{\beta/(1-\beta)}$	$\frac{1}{2}\,\frac{\beta}{1-\beta}$	$\frac{(3-2\beta)\,\beta}{1-\beta}$
Osipkov-Merritt (eq. [45])	$\left(\frac{s}{a}\right)^2 \frac{r^2+a^2}{s^2+a^2}\,\exp\left(\frac{r^2-s^2}{2\,a^2}\right)$	$\left(\frac{s}{a}\right)^2 \exp\left(\frac{r^2-s^2}{2\,a^2}\right)$	$\frac{r}{a}$	$\left(\frac{r}{a}\right)^2\,\frac{r^2+5\,a^2}{r^2+a^2}$
Mamon-Łokas (eq. [49])	$\frac{r+a}{s+a}\left(\frac{s}{s+2a}\right)$	$\frac{(r+2\,a)\,s}{(s+2\,a)^2}$	$\left(\frac{r}{a}\right)\,\frac{r+2\,a}{a}$	$\frac{2\,r}{a+r}$
Diemand-Moore-Stadel (eq. [58])	$s^{1/3}\frac{\left(a^{1/3}-s^{1/3}\right)^3}{\left(a^{1/3}-r^{1/3}\right)^4}$	$s^{1/3}\frac{\left(a^{1/3}-s^{1/3}\right)^2}{\left(a^{1/3}-r^{1/3}\right)^3}$	$\frac{r}{\left(a^{1/3}-r^{1/3}\right)^3}$	$\frac{2}{3}\left(\frac{r}{a}\right)^{1/3}\frac{5\,a^{1/3}-3\,r^{1/3}}{a^{1/3}-r^{1/3}}$

Notes: the Diemand-Moore-Stadel values are restricted to $r < a$.

which is provided again in Table 2 for our simple anisotropy models. The radial pressure is then simply $p(r) = p_\theta(r)/[1-\beta(r)]$.

The expressions for the dynamical pressure (radial or tangential) are made of single integrals involving $p_{\rm iso}$, which is a single integral itself. Hence, the dynamical pressure is expressed in terms of double integrals. For simple anisotropy profiles, we can simplify the dynamical pressure to single integrals by inserting the expression for $p_{\rm iso}(s)$ (eq. [10]) in equation (32) and inverting the order of integration. This yields

$$\begin{aligned} p_\theta(r) &= p_{\rm iso}(r) + \frac{1}{\pi}\int_r^\infty \frac{\mathrm{d}P}{\mathrm{d}R}\,\mathrm{d}R \int_r^R \frac{\beta}{1-\beta}\,\exp\left(-\int_r^s \frac{\beta}{1-\beta}\,\frac{\mathrm{d}t}{t}\right)\,\frac{\mathrm{d}s}{s\,\sqrt{R^2-s^2}} \\ &= p_{\rm iso}(r) + \frac{1}{\pi}\int_r^\infty P'(R)\mathrm{d}R \int_r^R B_\beta(r,s)\,\frac{\mathrm{d}s}{s\,\sqrt{R^2-s^2}} \end{aligned} \qquad (34)$$

and for simple $\beta(r)$, the inner integral can be expressed in closed form, as we shall now see.

2.3.2 *Case of finite β = cst < 1*

Equation (29) with A_β from Table 2 leads to

$$p(r) = \frac{p_{\rm iso}(r)}{1-\beta(r)} - \frac{\beta}{(1-\beta)^2}\,r^{\beta/(1-\beta)}\int_r^\infty p_{\rm iso}\,s^{-\beta/(1-\beta)}\,\frac{\mathrm{d}s}{s}\;. \qquad (35)$$

Using equation (34) with B_β from Table 2, one obtains a single integral representation for the tangential dynamical pressure

$$\begin{aligned} p_\theta(r) &= p_{\rm iso}(r) + \frac{1}{\pi}\,\frac{\beta}{1-\beta}\,r^{\beta/(1-\beta)}\int_r^\infty \frac{\mathrm{d}P}{\mathrm{d}R}\,\mathrm{d}R\int_r^R s^{-\beta/(1-\beta)}\,\frac{\mathrm{d}s}{s\,\sqrt{R^2-s^2}} \\ &= p_{\rm iso}(r) + \frac{1}{2\,\pi}\,\frac{\beta}{1-\beta}\,\frac{1}{r}\int_r^\infty \frac{\mathrm{d}P}{\mathrm{d}R}\,K_{\rm cst}\left(\frac{r}{R}\right)\,\mathrm{d}R\,, \end{aligned} \qquad (36)$$

where the second equality of equation (36) is obtained with the change of variable $t = 1 - s^2/R^2$. The dimensionless kernel in equation (36) is

$$K_{\rm cst}(u) = u^{1/(1-\beta)}\,B\left(1-u^2, \frac{1}{2}, -\frac{\beta/2}{1-\beta}\right)\;, \qquad (37)$$

where $B(x,a,b) = \int_0^x t^{a-1}\,(1-t)^{b-1}\mathrm{d}t$ is the incomplete Beta function. Integrating by parts the integral in equation (36), we finally obtain after some algebra a single integral expression for the tangential pressure that does not depend on derivatives of the observations:

$$p_\theta(r) = p_{\rm iso}(r) + \frac{1}{2\,\pi}\,\frac{\beta}{(1-\beta)^2}\left[r^{\beta/(1-\beta)}\int_r^\infty P(R)\,R^{-(2-\beta)/(1-\beta)}\,B\left(1-\frac{r^2}{R^2}, \frac{1}{2}, -\frac{\beta/2}{1-\beta}\right)\,\mathrm{d}R - 2(1-\beta)\int_r^\infty \frac{P(R)}{\sqrt{R^2-r^2}}\,\frac{\mathrm{d}R}{R}\right]. \qquad (38)$$

The surface term $R^{-1/(1-\beta)}\,B\left[1-r^2/R^2, 1/2, -\beta/(2\,(1-\beta))\right]\,P(R)$ that occurs in the integration by parts goes to 0 as $R\to\infty$. Indeed, for $x = r/R$ and $c = -\beta/2/(1-\beta)$, one has $x^{1-2c}\,B(1-x^2, 1/2, c) = -x/c + O(x^3)$ and moreover $P \to 0$. In practice, if a programming language does not provide the incomplete Beta function, but only the regularized incomplete Beta function, as $I(x,a,b) = B(x,a,b)/B(a,b) = \Gamma(a+b)B(x,a,b)/[\Gamma(a)\Gamma(b)]$, one should then be careful that $\Gamma(b)$ diverges when the last term b in the incomplete

Beta function is a negative integer, i.e. when $\beta = 2n/(2n+1) = 2/3, 4/5, 6/7...$ (n being a positive integer). Luckily, $B(x, a, b)$ always converges to finite values.[5]

In the limit $\beta \to 0$ everywhere, equations (35), (36), and (38) all reduce to $p(r) = p_{\rm iso}(r)$, as expected.

2.3.3 *Case of radial orbits:* $\beta = 1$

For radial orbits, differentiation of equation (23) leads to

$$p(r) = -r\, p'_{\rm iso}(r) = \frac{1}{\pi} \int_r^\infty \frac{{\rm d}^2 P}{{\rm d}R^2} \frac{R\,{\rm d}R}{\sqrt{R^2-r^2}} \ . \tag{39}$$

2.3.4 *Case of circular orbits:* $\beta \to -\infty$

For circular orbits, we proceed in a similar fashion: inserting the projected pressure (eq. [15]) into the definition of J (eq. [16]), one finds

$$\begin{aligned} J(r) &= 2 \int_r^\infty \frac{R^3\,{\rm d}R}{\sqrt{R^2-r^2}} \int_R^\infty p_\theta \frac{{\rm d}s}{s\sqrt{s^2-R^2}} \ , \\ &= \frac{\pi}{2} \int_r^\infty p_\theta \left(r^2+s^2\right) \frac{{\rm d}s}{s} \ , \end{aligned} \tag{40}$$

and

$$\frac{{\rm d}J}{{\rm d}r} = -\pi\, r \left(p_\theta - \int_r^\infty p_\theta \frac{{\rm d}s}{s} \right) \ . \tag{41}$$

Equations (22) and (41) lead to

$$-\frac{\rm d}{{\rm d}r} \left(\frac{1}{\pi r} \frac{{\rm d}J}{{\rm d}r} \right) = p'_\theta + \frac{p_\theta}{r} = p'_{\rm iso} = \frac{1}{f} \frac{{\rm d}\left(f\, p_\theta\right)}{{\rm d}r} \ , \tag{42}$$

whose solution is given by $f = r$:

$$p_\theta(r) = -\frac{1}{r} \int_r^\infty p'_{\rm iso}\, s\, {\rm d}s = p_{\rm iso}(r) + \frac{1}{r} \int_r^\infty p_{\rm iso}\, {\rm d}s \ , \tag{43}$$

where the 2nd equality is found by integration by parts, for which the surface term, $\lim_{r\to\infty} r\, p_{\rm iso}(r)$, vanishes for ${\rm d}\ln\rho/{\rm d}\ln r + {\rm d}\ln M/{\rm d}\ln r < 0$ (as derived from the Jeans equation [3]), as is the case for reasonable mass and tracer density profiles. Inserting $p_{\rm iso}$ (eq. [10]) into equation (43) and inverting the order of integration, we finally obtain the single integral expression for the tangential pressure:

$$p_\theta(r) = -\frac{1}{\pi} \int_r^\infty \frac{{\rm d}P}{{\rm d}R} \left[\frac{1}{\sqrt{R^2-r^2}} + \frac{1}{r} \cos^{-1}\left(\frac{r}{R}\right) \right] {\rm d}R \ . \tag{44}$$

2.3.5 *Case of Osipkov-Merritt anisotropy*

For the Osipkov-Merritt (Osipkov 1979; Merritt 1985) anisotropy

$$\beta(r) = \frac{r^2}{r^2+a^2} \ , \tag{45}$$

equations (31) reduces to

$$p_\theta(r) = -\int_r^\infty \exp\left(-\frac{s^2-r^2}{2\,a^2}\right) p'_{\rm iso}\, {\rm d}s = \left(\rho\,\sigma_r^2\right)_{\rm iso}(r) - \frac{1}{a^2} \int_r^\infty \exp\left(\frac{r^2-s^2}{2\,a^2}\right) p_{\rm iso}\, s\, {\rm d}s \ , \tag{46}$$

where the last equality is again obtained after integration by parts or from equation (32). Equation (34) yields (see Table 2) a single integral representation for the tangential dynamical pressure:

$$\begin{aligned} p_\theta(r) &= p_{\rm iso}(r) + \frac{1}{\pi a^2} \exp\left(\frac{r^2}{2a^2}\right) \int_r^\infty \frac{{\rm d}P}{{\rm d}R} {\rm d}R \int_r^R \exp\left(-\frac{s^2}{2a^2}\right) \frac{s\,{\rm d}s}{\sqrt{R^2-s^2}} \\ &= p_{\rm iso}(r) + \frac{1}{\pi\, a} \int_r^\infty \frac{{\rm d}P}{{\rm d}R} K_{\rm OM}\left(\sqrt{\frac{R^2-r^2}{2\,a^2}}\right) {\rm d}R \ , \end{aligned} \tag{47}$$

where the dimensionless kernel $K_{\rm OM}$ is

$$K_{\rm OM}(u) = \sqrt{2}\, F(u) = \sqrt{\frac{\pi}{2}} \exp\left(-u^2\right) {\rm erfi}\, u \ , \tag{48}$$

---

[5] An SM macro for $B(x, a, b)$ is available upon request.

where

$$F(u) = \frac{\sqrt{\pi}}{2}\,\exp\left(-u^2\right) \mathrm{erfi}\,u = \frac{\sqrt{\pi}\,\exp\left(-u^2\right)\,\mathrm{erf}(iu)}{2\,i}$$

is Dawson's integral and where $\mathrm{erfi}(x)$ is the imaginary error function. Note that Dawson's integral is available in most software packages for mathematical functions.[6] Equation (47) can also be found by inserting the expression for $p_{\rm iso}(s)$ (eq. [10]) into equation (46) and reversing the order of integration.

2.3.6 *Case of Mamon-Łokas anisotropy*

For the simple anisotropy profile that Mamon & Łokas (2005b) found to fit well ΛCDM halos

$$\beta(r) = \frac{1}{2}\,\frac{r}{r+a}\ , \tag{49}$$

one obtains

$$p_\theta(r) = -\,(r+2\,a)\int_r^\infty p'_{\rm iso}\,\frac{\mathrm{d}s}{s+2\,a} = p_{\rm iso}(r) - (r+2\,a)\int_r^\infty p_{\rm iso}\,\frac{\mathrm{d}s}{(s+2\,a)^2}\ , \tag{50}$$

where the first equality is from equation (31), while the second one is obtained after integration by parts or from equation (32). Equation (34) now yields (see Table 2) the single integral expression for the tangential dynamical pressure:

$$\begin{aligned} p_\theta(r) = \frac{r/2+a}{r+a}\,\rho(r)\,\sigma_r^2(r) &= p_{\rm iso}(r) + \frac{1}{\pi}\,(r+2\,a)\int_r^\infty \frac{\mathrm{d}P}{\mathrm{d}R}\int_r^R \frac{\mathrm{d}s}{(s+2\,a)^2\,\sqrt{R^2-s^2}} \\ &= p_{\rm iso}(r) + \frac{1}{\pi}\,\frac{r+2\,a}{a^2}\int_r^\infty \frac{\mathrm{d}P}{\mathrm{d}R}\,K_{\rm ML}\left(\frac{R}{a},\frac{r}{a}\right)\,\mathrm{d}R\ , \end{aligned} \tag{51}$$

where the dimensionless kernel $K_{\rm ML}$, using $X=R/a$, $x=r/a$ and $y=s/a$, is

$$\begin{aligned} K_{\rm ML}(X,x) &= \int_x^X \frac{\mathrm{d}y}{\sqrt{X^2-y^2}\,(y+2)^2} \\ &= \frac{1}{X^2}\int_0^{\cos^{-1}(x/X)} \frac{\mathrm{d}\theta}{(\cos\theta+2/X)^2} \end{aligned} \tag{52}$$

$$= \begin{cases} -\dfrac{1}{4-X^2}\,\dfrac{\sqrt{X^2-x^2}}{2+x} + \dfrac{4}{(4-X^2)^{3/2}}\,\tan^{-1}\left[\sqrt{\dfrac{2-X}{2+X}}\,\sqrt{\dfrac{X-x}{X+x}}\right] & \text{for } X<2\ , \\ \dfrac{1}{12}\,\dfrac{(4+x)\,\sqrt{2-x}}{(2+x)^{3/2}} & \text{for } X=2\ , \\ \dfrac{1}{X^2-4}\,\dfrac{\sqrt{X^2-x^2}}{2+x} - \dfrac{4}{(X^2-4)^{3/2}}\,\tanh^{-1}\left[\sqrt{\dfrac{X-2}{X+2}}\,\sqrt{\dfrac{X-x}{X+x}}\right] & \text{for } X>2\ , \end{cases} \tag{53}$$

where equation (52) is found through the variable substitution $y = X\,\cos\theta$. Equations (51) and (52) can also be found by inserting the expression for $p_{\rm iso}$ (eq. [10]) into equation (50) and reversing the order of integration.

2.3.7 *Case of generalized Mamon-Łokas anisotropy*

The velocity anisotropies in halos in cosmological N body simulations do not always fit the Mamon-Łokas formula (eq. [49]), but instead, $\beta(r)$ shows halo to halo variations in its limits at $r=0$ and $r\to\infty$ (Wojtak et al. 2008). Hence, a more general form for the anisotropy profile is (e.g. Tiret et al. 2007)

$$\beta(r) = \beta_0 + (\beta_\infty-\beta_0)\,\frac{r}{r+a}\ . \tag{54}$$

The Mamon-Łokas anisotropy is the special case with $\beta_0=0$ and $\beta_\infty=1/2$. For $\beta_0<1$ and $\beta_\infty<1$, inserting equation (54) into equation (31) yields, after some algebra:

$$\begin{aligned} p_\theta(r) &= -r^{\beta_0/(1-\beta_0)}\,\left[(1-\beta_\infty)\,r + (1-\beta_0)\,a\right]^{\beta_\infty/(1-\beta_\infty)-\beta_0/(1-\beta_0)} \\ &\quad\times\int_r^\infty s^{-\beta_0/(1-\beta_0)}\,\left[(1-\beta_\infty)\,s + (1-\beta_0)\,a\right]^{\beta_0/(1-\beta_0)-\beta_\infty/(1-\beta_\infty)}\,p'_{\rm iso}\,\mathrm{d}s\ . \end{aligned} \tag{55}$$

For $\beta_0<\beta_\infty=1$, the same procedure gives

---

[6] SM macros for $\mathrm{erfi}(x)$ and Dawson's $F(x)$ are available upon request.

$$p_\theta(r) = -\exp\left(\frac{r/a}{1-\beta_0}\right) r^{\beta_0/(1-\beta_0)} \int_r^\infty \exp\left(-\frac{s/a}{1-\beta_0}\right) s^{-\beta_0/(1-\beta_0)}\, p'_{\rm iso}\, {\rm d}s\ . \tag{56}$$

For $\beta_\infty < \beta_0 = 1$,[7] we similarly obtain

$$p_\theta(r) = -\exp\left(-\frac{a/r}{1-\beta_\infty}\right) r^{\beta_\infty/(1-\beta_\infty)} \int_r^\infty \exp\left(\frac{a/s}{1-\beta_\infty}\right) s^{-\beta_\infty/(1-\beta_\infty)}\, p'_{\rm iso}\, {\rm d}s\ . \tag{57}$$

The integrals of equations (55), (56), and (57), are essentially double integrals, since they involve $p'_{\rm iso}$ (eq. [12]). Single integral solutions do not appear to be possible to derive, even for the simple case of $\beta_0 = 0$ (unless $\beta_\infty = 1/2$, i.e. the Mamon-Łokas anisotropy model).

2.3.8 *Case of Diemand-Moore-Stadel anisotropy*

Finally for the other simple anisotropy profile that Diemand, Moore, & Stadel (2004, Sect. 3.3.2) also found to fit well ΛCDM halos

$$\beta(r) = \begin{cases} \left(\dfrac{r}{a}\right)^{1/3} & r < a\ , \\ 1 & r \geqslant a\ , \end{cases} \tag{58}$$

we obtain

$$\begin{array}{lll} p_\theta(r) & = p_{\rm iso}(r) - \dfrac{1}{\left(a^{1/3}-r^{1/3}\right)^3} \displaystyle\int_r^a p_{\rm iso} \left(a^{1/3}-s^{1/3}\right)^2 \frac{{\rm d}s}{s^{2/3}} & \text{for } r < a\ , \\ p(r) & = p_{\rm rad}(r) & \text{for } r \geqslant a\ , \end{array} \tag{59}$$

where equation (59) is obtained from equation (32), while the equation (59) comes from the pure radial orbits for $r \geqslant a$ (eq. [58]). Again, for $r < a$, the integral in equation (59) is essentially a double integral (because of $p'_{\rm iso}$), and a single integral solution can be obtained using equation (34), yielding (with Table 2)

$$\begin{aligned} p_\theta(r) &= p_{\rm iso}(r) + \frac{1}{\pi\left(a^{1/3}-r^{1/3}\right)^3} \int_r^a \frac{{\rm d}P}{{\rm d}R}\,{\rm d}R \int_r^R \frac{\left(a^{1/3}-s^{1/3}\right)^2}{s^{2/3}\sqrt{R^2-s^2}}\,{\rm d}s \\ &= p_{\rm iso}(r) + \frac{1}{\pi\left(a^{1/3}-r^{1/3}\right)^3} \int_r^a \frac{{\rm d}P}{{\rm d}R}\, K_{\rm DMS}\left(\frac{R}{a},\frac{r}{a}\right) {\rm d}R\ , \end{aligned} \tag{60}$$

where the dimensionless kernel is

$$\begin{aligned} K_{\rm DMS}(X,x) &= \int_x^X \frac{\left(1-y^{1/3}\right)^2}{\sqrt{X^2-y^2}} \frac{{\rm d}y}{y^{2/3}} \\ &= \frac{1}{X^{2/3}} \int_0^{\cos^{-1}(x/X)} \frac{{\rm d}\theta}{\cos^{2/3}\theta} - \frac{2}{X^{1/3}} \int_0^{\cos^{-1}(x/X)} \frac{{\rm d}\theta}{\cos^{1/3}\theta} + \int_0^{\cos^{-1}(x/X)} {\rm d}\theta \\ &= \left[\sqrt{\pi}\,\frac{\Gamma(1/6)}{\Gamma(2/3)} - B\left(\frac{x^2}{X^2},\frac{1}{6},\frac{1}{2}\right)\right] \frac{X^{-2/3}}{2} - \left[\sqrt{\pi}\,\frac{\Gamma(1/3)}{\Gamma(5/6)} - B\left(\frac{x^2}{X^2},\frac{1}{3},\frac{1}{2}\right)\right] X^{-1/3} + \cos^{-1}\left(\frac{x}{X}\right)\ , \end{aligned} \tag{61}$$

for $X = R/a$, $x = r/a$ and $y = s/a$.

2.3.9 *General expression for the tangential pressure for specific anisotropy profiles*

The expressions for the tangential pressure for the cases of constant, Osipkov-Merritt, Mamon-Łokas, and Diemand-Moore-Stadel anisotropy (eqs. [36], [47], [51], and [60], respectively) can all be written in the form

$$p_\theta(r) = p_{\rm iso}(r) + \frac{1}{\pi\, r}\, C_\beta(r) \int_r^\infty \frac{{\rm d}P}{{\rm d}R} K_\beta\, {\rm d}R = \frac{1}{\pi\, r} \int_r^\infty \frac{{\rm d}P}{{\rm d}R} \left[C_\beta(r)\, K_\beta\left(\frac{R}{a},\frac{r}{a}\right) - \frac{r}{\sqrt{R^2-r^2}}\right] {\rm d}R\ , \tag{62}$$

where the second equality of equation (62) is found with equation (10) and where $C_\beta(r)$ and $K_\beta(X,x)$ are dimensionless functions such that

$$C_\beta(r)\, K_\beta\left(\frac{R}{a},\frac{r}{a}\right) = r \int_r^\infty \frac{B_\beta(r,s)}{\sqrt{r^2-s^2}} \frac{{\rm d}y}{y}\ , \tag{63}$$

with $C_\beta(r)$ given in Table 2, and K_β given in equations (37), (48), (53) and (61), respectively. For the Diemand-Moore-Stadel anisotropy model, the upper integration limits in equation (62) should be replaced by the anisotropy radius a. The second equality of equation (62) allows the kinematic deprojection with a unique single integral.

---

[7] Decreasing anisotropy profiles are found for some regular halos (Wojtak et al. 2008), although the central anisotropy is never unity.

2.4 Mass profiles of spherical systems with arbitrary known anisotropy

2.4.1 General mass profile

The mass profile is obtained through stationary non-streaming spherical Jeans equation (3), which writes

$$-\,\rho \frac{GM}{r^2} = p' + \frac{2}{r}\,\beta\, p\,. \tag{64}$$

Now, equation (24) reads

$$p' = \frac{p'_{\rm iso}}{1-\beta} + \frac{r\,\beta' + \beta}{1-\beta}\,\frac{p}{r} = \frac{p'_{\rm iso}}{1-\beta} + \frac{r\,\beta' + \beta}{(1-\beta)^2}\,\frac{p_\theta}{r}\,. \tag{65}$$

Inserting p' from equation (65) into equation (64) yields the *general mass inversion equation* (dropping the dependencies on r for clarity):

$$-\,(1-\beta)\,\rho\,\frac{GM}{r^2}(r) = p'_{\rm iso}(r) + \left[\frac{\beta' + (3-2\,\beta)\,\beta/r}{1-\beta}\right]\,p_\theta(r) = p'_{\rm iso}(r) + \frac{D_\beta(r)}{r}\,p_\theta(r)\,, \tag{66}$$

where the dimensionless function

$$D_\beta(r) = \frac{r\,{\rm d}\beta/{\rm d}r + (3-2\,\beta)\,\beta}{1-\beta} \tag{67}$$

is given in Table 2 for four anisotropy models. Inserting the general expression for p_θ into equation (66), and converting the mass into the circular velocity with $v_c^2(r) = G\,M(r)/r$ gives either

$$[1-\beta(r)]\,\rho(r)\,v_c^2(r) = -r\,p'_{\rm iso}(r) + \left[\frac{r\,\beta' + (3-2\,\beta)\,\beta}{1-\beta}\right]\,\left[\int_r^\infty p_{\rm iso}\,\frac{\beta}{1-\beta}\,\exp\left(-\int_r^s \frac{\beta}{1-\beta}\,\frac{{\rm d}t}{t}\right)\,\frac{{\rm d}s}{s} - p_{\rm iso}\right]\,, \tag{68}$$

(from eq. [29]) or

$$[1-\beta(r)]\,\rho(r)\,v_c^2(r) = \left[\frac{r\,\beta' + (3-2\,\beta)\,\beta}{1-\beta}\right]\,\int_r^\infty \exp\left(-\int_r^s \frac{\beta}{1-\beta}\,\frac{{\rm d}t}{t}\right)\,p'_{\rm iso}\,{\rm d}s - r\,p'_{\rm iso}(r) \tag{69}$$

(from eq. [28]). Alas, both forms (eqs. [68] and [69]) involve the second derivative of the observable P, hence the second form (eq. [69]) seems preferable to use as it is simpler. However, for simple anisotropy profiles, the double integral of equations (68) and (69) can be simplified to single integrals, or equivalently, single integral expressions for p_θ exist, which can be inserted into equation (66) to obtain a single integral expression for the mass profile.

2.4.2 Case of isotropic systems

For isotropic systems ($\beta = 0$), equation (66) trivially leads to

$$v_c^2(r) = -\frac{r p'_{\rm iso}(r)}{\rho(r)}\,, \tag{70}$$

which is equivalent to the first equality of equation (11).

2.4.3 Case of finite $\beta = {\rm cst} < 1$

For finite $\beta = {\rm cst} < 1$, while equation (69) becomes (with D_β from Table 2)

$$-\,(1-\beta)\;\rho\,\frac{GM}{r^2}(r) = p'_{\rm iso} - \left[\frac{\beta\,(3-2\,\beta)/r}{1-\beta}\right]\;r^{\beta/(1-\beta)}\,\int_r^\infty s^{-\beta/(1-\beta)}\,p'_{\rm iso}\,{\rm d}s\,, \tag{71}$$

a single integral expression is found inserting the tangential pressure (eq. [38]) into equation (66) to yield

$$\begin{aligned} -\,(1-\beta)\,\rho\,\frac{GM}{r^2}(r) \;\; &= \;\; p'_{\rm iso} + \left[\frac{\beta\,(3-2\,\beta)/r}{1-\beta}\right]\,\Bigg\{p_{\rm iso} + \frac{1}{2\pi}\,\frac{\beta}{(1-\beta)^2} \\ &\times \left[r^{\beta/(1-\beta)}\int_r^\infty P(R)\,R^{-(2-\beta)/(1-\beta)}\,B\left(1-\frac{r^2}{R^2},\frac{1}{2},-\frac{\beta/2}{1-\beta}\right)\,{\rm d}R - 2(1-\beta)\int_r^\infty \frac{P(R)}{\sqrt{R^2-r^2}}\,\frac{{\rm d}R}{R}\right]\Bigg\}\,. \end{aligned} \tag{72}$$

2.4.4 Case of radial orbits: $\beta = 1$

For radial anisotropy, equations (39) and (64) simply yield

$$\rho(r)\,\frac{GM(r)}{r^2} = 3\,p'_{\rm iso} + r\,p''_{\rm iso}\,.$$

However, using the change of variables $R = r\cosh u$, the last equality of equation (39) yields

$$p'_{\rm rad} = \frac{p_{\rm rad}}{r} + \frac{1}{\pi r} \int_r^\infty P''' R^2 \, \frac{{\rm d}R}{\sqrt{R^2-r^2}} \,, \tag{73}$$

hence, from equation (64):

$$v_c^2(r) = -\frac{1}{\pi \, \rho(r)} \int_r^\infty \left(3\,P'' + R\,P'''\right) \frac{R\,{\rm d}R}{\sqrt{R^2-r^2}} \,. \tag{74}$$

Alas, equation (74) involves a triple differentiation of the observables.

2.4.5 *Case of circular orbits: $\beta \to -\infty$*

For circular orbits, the first term in the stationary non-streaming spherical Jeans equation (3) vanishes, and one is left with the trivial relation

$$v_c^2(r) = 2\,\sigma_\theta^2 = \frac{2}{\rho(r)} \left[p_{\rm iso} + \frac{1}{r} \int_r^\infty p_{\rm iso}\,{\rm d}s\right] \,, \tag{75}$$

where we made use of equation (43) for the last equality. Integrating the last equation by parts, or equivalently, using equation (44), we get

$$v_c^2(r) = -\frac{2}{\pi \, \rho(r)} \int_r^\infty \frac{{\rm d}P}{{\rm d}R} \left[\frac{1}{\sqrt{R^2-r^2}} + \frac{1}{r} \, \cos^{-1}\left(\frac{r}{R}\right)\right] {\rm d}R \,. \tag{76}$$

2.4.6 *Case of Osipkov-Merritt anisotropy*

For Osipkov-Merritt anisotropy (eq. [45]), equation (66) leads to (with D_β from Table 2)

$$\rho \, \frac{GM}{r^2}(r) = -\frac{r^2+a^2}{a^2} \, p'_{\rm iso} + \frac{1}{a^2} \left(\frac{r^2+a^2}{a^2} + 4\right) r \int_r^\infty \exp\left(\frac{r^2-s^2}{2\,a^2}\right) p'_{\rm iso}\,{\rm d}s \,. \tag{77}$$

A single integral solution to the mass profile is obtained by inserting p_θ of equation (47) into equation (66), yielding

$$-\,\rho \, \frac{GM}{r^2}(r) = \frac{r^2+a^2}{a^2} \, p'_{\rm iso} + \left(r^2 + 5\,a^2\right) \frac{r}{a^5} \left[p_{\rm iso}\,a + \frac{1}{\sqrt{2\pi}} \, \exp\left(\frac{r^2}{2a^2}\right) \int_r^\infty \frac{{\rm d}P}{{\rm d}R} \, \exp\left(-\frac{R^2}{2a^2}\right) \, {\rm erfi}\sqrt{\frac{R^2-r^2}{2a^2}} \, {\rm d}R\right] \,. \tag{78}$$

2.4.7 *Case of Mamon-Łokas anisotropy*

For Mamon & Łokas anisotropy (eq. [49]), equation (66) brings (with D_β from Table 2)

$$\rho \, \frac{GM}{r^2}(r) = -2\,\frac{r+a}{r+2\,a} \, p'_{\rm iso} + 4 \int_r^\infty p'_{\rm iso} \, \frac{{\rm d}s}{s+2\,a} \,. \tag{79}$$

The single integral solution, found by inserting p_θ from equation (51) into equation (66), is

$$-\,\rho \, \frac{GM}{r^2}(r) = \frac{2}{r+2\,a} \, \left[(r+a)\,p'_{\rm iso} + 2\,p_{\rm iso}\right] + \frac{4}{\pi\,a^2} \int_r^\infty \frac{{\rm d}P}{{\rm d}R} \, K_{\rm ML}\left(\frac{R}{a},\frac{r}{a}\right) {\rm d}R \,, \tag{80}$$

where the dimensionless kernel $K_{\rm ML}$ is given in equation (53).

2.4.8 *Case of Diemand-Moore-Stadel anisotropy*

Finally for the anisotropy profile (eq. [58]) proposed by Diemand et al. (2004), equation (66) leads to (with D_β from Table 2)

$$-\left(\frac{a^{1/3}-r^{1/3}}{a^{1/3}}\right) \rho \, \frac{GM}{r^2}(r) = p'_{\rm iso} - \frac{2/3}{\left(a\,r^2\right)^{1/3}} \left(\frac{5\,a^{1/3}-3\,r^{1/3}}{a^{1/3}-r^{1/3}}\right) \left[p_{\rm iso} + \frac{1/\pi}{\left(a^{1/3}-r^{1/3}\right)^3} \int_r^a \frac{{\rm d}P}{{\rm d}R} \, K_{\rm DMS}\left(\frac{R}{a},\frac{a}{a}\right) {\rm d}R\right] \,, \tag{81}$$

for $r < a$, and to the radial solution (eq. [74]) for $r > a$.

2.4.9 *General form of the mass profile for specific anisotropy profiles*

Inserting equations (12) and (62) into equation (66), one can obtain a general form for the mass profiles for the constant anisotropy, Osipkov-Merritt, Mamon-Łokas, and Diemand-Moore-Stadel anisotropy profiles:

$$-\left[1-\beta(r)\right] \rho(r) \frac{GM(r)}{r^2} = \frac{1}{\pi\,r} \int_r^\infty \left\{\frac{D_\beta(r)}{r} \left[C_\beta(r)\,K_\beta - \frac{r}{\sqrt{R^2-r^2}}\right] \frac{{\rm d}P}{{\rm d}R} - \frac{R}{\sqrt{R^2-r^2}} \, \frac{{\rm d}^2P}{{\rm d}R^2}\right\} {\rm d}R \,, \tag{82}$$

where, for the Diemand-Moore-Stadel anisotropy profile, the anisotropy radius a should be used for the upper integration limits. Equation (82) allows to express the mass profile as a unique single integral of the observations, where $C_\beta(r)$ and $D_\beta(r)$ are given in Table 2, while the kernel K_β is given by equations (37), (48), (53), and (61) for the constant anisotropy, Osipkov-Merritt, Mamon-Łokas, and Diemand-Moore-Stadel anisotropy models, respectively. Equivalently, equation (82) can be used to formulate the circular velocity profile

$$v_c^2(r) = \frac{1}{\pi\,[1-\beta(r)]\,\rho(r)} \int_r^\infty \left\{ \frac{R}{\sqrt{R^2-r^2}} \frac{\mathrm{d}^2 P}{\mathrm{d}R^2} - \frac{D_\beta(r)}{r} \left[C_\beta(r)\,K_\beta(R,r) - \frac{r}{\sqrt{R^2-r^2}} \right] \frac{\mathrm{d}P}{\mathrm{d}R} \right\} \mathrm{d}R\,. \qquad (83)$$

For isotropic models, equation (83) with $D_\beta = C_\beta = K_\beta = 0$ recovers the second equality in equation (14).

In practice, writing the tracer density as $\rho(r) = \rho(a)\,\widetilde{\rho}(r/r_s)$, where r_s is the characteristic scale of the tracer, the projected pressure as $P(R) = P(r_s)\,\widetilde{P}(R/r_s)$, equation (83) yields

$$\begin{aligned}
\left[\frac{v_c(r)}{\sigma_{\rm los}(r_s)}\right]^2 &= \frac{\Sigma(r_s)/\left[\pi\,r_s\,\rho(r_s)\right]}{[1-\beta(r)]\,\widetilde{\rho}(r/r_s)} \int_x^\infty \left\{ \frac{X}{\sqrt{X^2-x^2}} \frac{\mathrm{d}^2\widetilde{P}}{\mathrm{d}X^2} - \frac{D_\beta(r_s x)}{x} \left[C_\beta(r_s x)\,K_\beta - \frac{x}{\sqrt{X^2-x^2}} \right] \frac{\mathrm{d}\widetilde{P}}{\mathrm{d}X} \right\} \mathrm{d}X\,, \\
&= \frac{\Sigma(r_s)}{\left[\pi\,r_s\,\rho(r_s)\right]}\,\frac{r/r_s}{[1-\beta(r)]\,\widetilde{\rho}(r/r_s)} \\
&\quad \times \int_0^{\cosh^{-1}(X_{\rm max}/x)} \widetilde{P}''(x\,\cosh u)\,\cosh u - \frac{D_\beta(r_s x)}{x}\,\left[C_\beta(r_s x)\,K_\beta(x\cosh u, x)\,\sinh u - 1\right]\,\widetilde{P}'(x\cosh u)\,du \qquad (84)
\end{aligned}$$

where $x = r/r_s$, $X = R/r_s$, and where the second equality of equation (84) is useful to avoid the singularity at $X = x$, integrating out to the equivalent of, say, $10\,r_v$, i.e. $X_{\rm max} = 10\,r_v/r_s$. All quantities on the right-hand side of the two equalities in equation (84) are known or assumed (the anisotropy profile). In particular, the numerator of the factor in front of the integral of the first equality of equation (84) is a function of the shape of the tracer density profile, found by Abel inversion (eq. [8]) of the surface density profile.

3 TESTS

3.1 Accuracy

We test our mass inversion equations, on four anisotropy models: isotropic, constant, Osipkov-Merritt and Mamon-Łokas. For each of these anisotropy models, we compute the projected pressure using equation (6), with the kernels given by Mamon & Łokas (2005b, 2006), evaluated on a logarithmic grid from $r = 0.01\,r_s$ to $100\,r_s$ in steps of 0.2 dex. The projected pressures $P(R)$ were differentiated after cubic spline interpolation and the integral of equation (83) was performed in steps of $\cosh^{-1}(R/r)$ out to $100\,r_s$. We choose our mass and anisotropy models by placing ourselves in the context of clusters of galaxies. We assume a one-component NFW model (Navarro et al. 1996), for which the dimensionless density and mass profiles can be expressed as

$$\begin{aligned}
\widetilde{\rho}(x) &= \frac{\rho(x r_s)}{M(r_s)/\left(4\pi r_s^3\right)} = \frac{(\ln 2 - 1/2)^{-1}}{x(x+1)^2}\,, \qquad (85) \\
\widetilde{M}(x) &= \frac{M(x r_s)}{M(r_s)} = \frac{\ln(x+1) - x/(x+1)}{\ln 2 - 1/2}\,, \qquad (86)
\end{aligned}$$

where r_s is the scale radius, where the slope of the density profile is -2. We make no use of our assumption that the total and tracer density profiles are proportional.

The anisotropy profile for dark matter particles in ΛCDM halos of the masses of clusters is close to the Mamon-Łokas model (Mamon & Łokas 2005b; Wojtak et al. 2008; Mamon et al. 2009) with anisotropy radius $a \simeq 0.18\,r_{200}$ (Mamon & Łokas) or $0.275\,r_{200} = 1.1\,r_s$ (Mamon et al.). We adopt a scaling of $a = r_s$ for the Mamon-Łokas model and for the Osipkov-Merritt model as well, and we adopt a constant anisotropy model that is fairly radial but consistent with the anisotropy seen in ΛCDM halos: $\beta = 0.4$.

Figure 1 shows the comparison of the circular velocity profiles obtained from the mass inversion equation (83) with the true circular velocity profiles. Despite the double differentiation of the projected pressure, the circular velocity (hence mass) profiles are recovered to a few percent relative accuracy or better,[8] except at the innermost point where the mass is overestimated by 4 to 10% in the four anisotropy models, because of the inaccurate cubic-spline interpolation of $P(R)$ near the edges. The accuracy of the mass inversion is even better if we use a finer grid to measure the projected pressure before the cubic spline interpolation of $P(R)$ and subsequent mass inversion: for example with the OM anisotropy, the maximum relative error in the recovered mass decreases with grid size from 9% (0.2 dex steps) to 0.6% (0.02 dex steps).

3.2 Robustness to small data samples

We next test the accuracy of the recovered mass profiles when the data is sparse and noisy. We consider the case of velocity measurements in a cluster of galaxies. We assume that the cluster has 500 measured velocities within $5\,r_s$ (which is roughly the cluster virial radius), and assume for simplicity that we have line-of-sight velocity dispersions measured in 10 equal size radial bins centered from 0.25 to $4.75\,r_s$. With $N = 50$ velocities per bin, the velocity dispersions are known to a relative accuracy of $\sqrt{1/2/(N-1)} = 10.1\%$ (e.g. Lupton 1993), and we fold this noise[9] into the predicted line-of-sight velocity dispersion profile, using the same seed for the random number generator for all four anisotropy profiles. We extrapolate the projected pressures to larger radii by fitting a power-law to $P(R)$ using the last 5 data

---

[8] Both mass inversion and deprojection appear to be unstable at radii $r < r_s$ for the Mamon-Łokas anisotropy model when a is exactly set to r_s, when using our `Mathematica` routines (but this odd behavior is not present when tested with other software). The figure shows the case $a = 1.001\,r_s$.

[9] We neglect the noise on the uncertain surface density profile, which contributes negligibly to the noise in the projected pressure in comparison to the noise in the velocity dispersion.

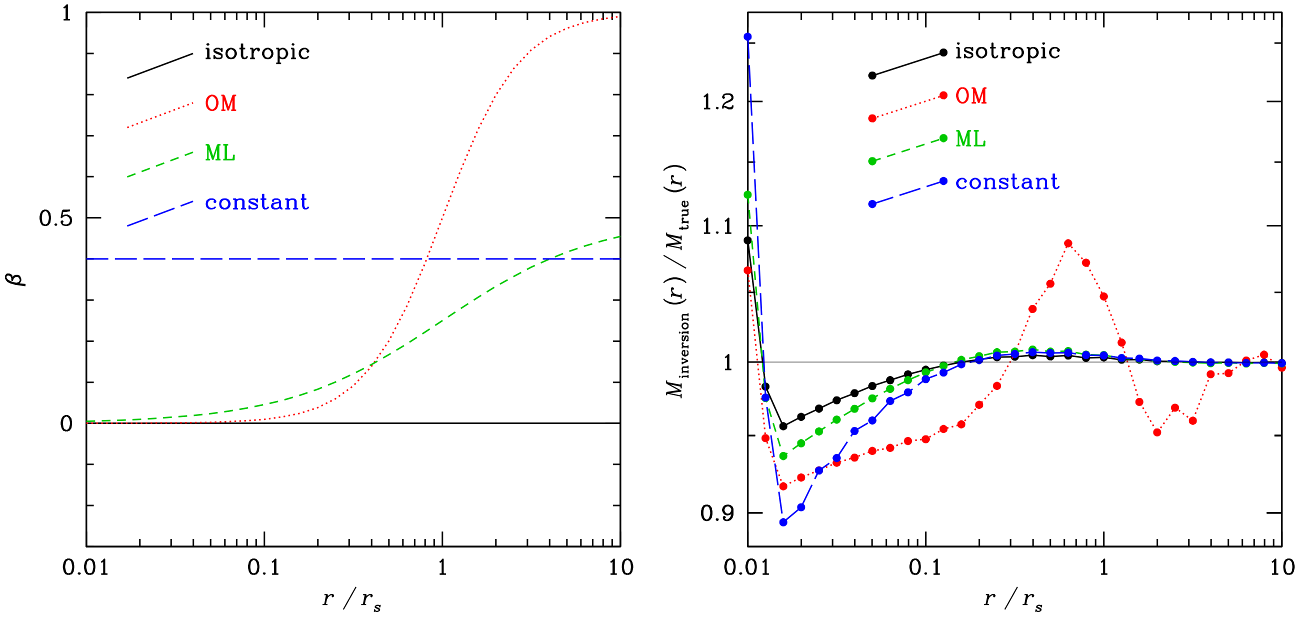

Figure 1. *Left:* Adopted anisotropy profiles: isotropic (*solid black line*), Osipkov-Merritt (eq. [45], with $a = r_s$, *dotted red line*), Mamon-Łokas (eq. [49], with $a = r_s$, *short dashed green line*), and $\beta = \mathrm{cst} = 0.4$ (*long dashed blue line*). *Right:* Accuracy of the mass inversion (in the absence of noise): ratio of inferred (eq. [83], using eq. [6] to first evaluate P on logarithmic grid of 0.2 dex steps, and using the dimensionless functions of Table 2, and the dimensionless kernels of equations [48], [53], and [37], for the latter three anisotropy models) over true NFW mass profiles for the four anisotropy models shown in the left panel.

points, at outer linearly spaced outer radii, with the same spacing as the data, and then fit a 4th order polynomial to the set of observed and mock-extrapolated data. We repeated these tests 5 times with different seeds for the random generator.

The left-hand panel of Figure 2 shows the accuracy of the mass inversion is much worse than in the academic case with no noise. In particular, the extrapolation errors at radii lower than the lowest data point make the inner mass profile inaccurate to factors often greater than 2. With the isotropic, $\beta = 0.4$, and Mamon-Łokas anisotropy models, the mass profile is nevertheless recovered to typically better than 20% accuracy for $r > 0.8\, r_s$, out to twice the radius of the last data point. However, the large error bars show that there is a large scatter in the accuracy of the recovered mass profile for different randomly generated projected pressure profiles. The right-hand panel of Figure 2 gives the second highest error among the five tests performed, for each given radius and anisotropy model. Typical such 80-percentile errors are of the order of 70% for $r > 0.8\, r_s$. Surprisingly, this typical error decreases to only 20% at high radii ($r > 8\, r_s$), despite the fact that the projected pressure is extrapolated beyond $r = 4.5\, r_s$.

3.3 Robustness to the wrong anisotropy model

The essential ingredient to the mass inversion is the knowledge of the velocity anisotropy profile. How wrong can the mass inversion be if the incorrect anisotropy profile is used? We adopt the Mamon-Łokas anisotropy model with $a = r_s$ similar to what is found for cluster-mass ΛCDM halos (Mamon et al. 2009) and compute the projected pressure for an NFW model with this anisotropy model. We then perform the mass inversion assuming other anisotropy profiles to see how off we are. In this exercise, we assume perfect data, i.e. no noise.

The left panel of Figure 3 shows that the mass profile is recovered to better than 33% accuracy for all anisotropy models at $r > 4\, r_s$, i.e. beyond the virial radius. Within the virial radius, the Osipkov-Merritt underestimates the mass by as much as a factor 3 around $2\, r_s$, but is much more precise at very low radii. The $\beta = 0.4$ model is accurate for $r > r_s$, as expected as it resembles there the Mamon-Łokas model, but underestimates the mass by increasingly large factors at radii $r < r_s$, and the recovered mass actually goes negative at $r < 0.17\, r_s$. Finally, the isotropic model finds the correct mass to within 30% at all radii, usually overestimating the true mass. Interestingly, at $r \simeq 7\, r_s$, all four anisotropy models lead to the correct mass to within 5%.

The right panel of Figure 3 indicates that the recovered mass is not very sensitive to the assumed anisotropy radius, as the mass is recovered to 20% accuracy, unless the anisotropy radius is assumed to be 10 times lower than it actually is. This graph also shows that at $r \simeq 3\, r_s$ (i.e. roughly two-thirds the virial radius of clusters), the mass is correctly recovered to better than 5% for our five choices of anisotropy radius.

4 DISCUSSION

The mass inversion algorithm presented in this work generally (eq. [69]), requires two steps: 1) deprojection and 2) inserting the radial pressure in the Jeans equation to derive the mass. The deprojection (eq. [32]) requires a single integral involving of a quantity, $p_{\rm iso}$ (eq. [10])

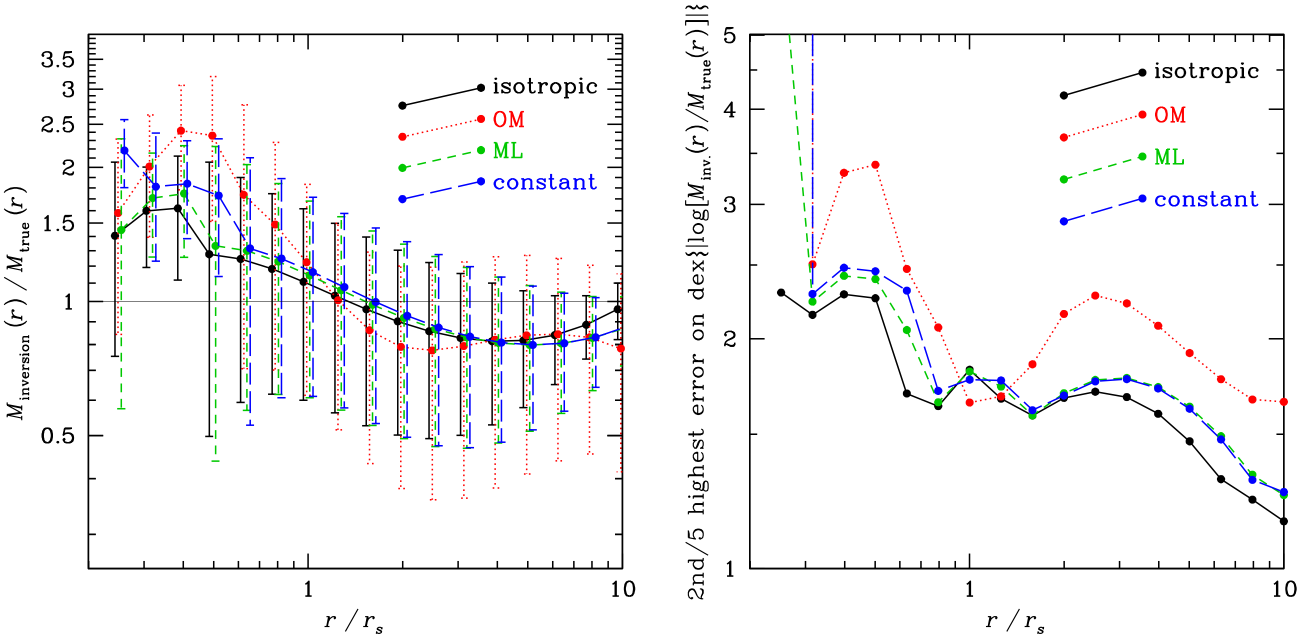

Figure 2. Robustness of the mass inversion to small data samples. *Left:* Same as right panel of Fig. 1, but for the projected pressure profile measured on a linear grid of 10 radial bins from 0.25 to $4.75\,r_s$, with 20% relative gaussian errors on the projected pressure (i.e. 10% errors on the line-of-sight velocity dispersion measurements based upon 50 velocities per radial bin). The error bars show the standard deviations on 5 tests with different seeds for the random number generator. The points and error bars are slightly shifted along the x-axis for clarity. *Right:* 2nd highest error out of 5 tests on recovered mass profile. A value of unity indicates a perfect recovery of the mass.

that is itself a single integral involving the derivative of the observed projected pressure. The second step (mass inversion) also requires a single integral involving the derivative of $p_{\rm iso}$. Each differentiation of the data introduces errors, and the full mass inversion requires three single integrals. For the special cases of simple anisotropy models, we find it preferable to write the mass profile with a single integral involving the double derivative of the observed projected pressure. Indeed, this requires a single smoothing operation before differentiation, thus leading to more accurate results, even if the mathematical formulation of the deprojections and mass inversions for each of the simple anisotropy models has strongly increased the number of equations in this article.

While this work (and Wolf et al. (2009)) used the Abel inversion for the kinematic deprojection, one can alternatively apply Fourier methods (see also Kalal & Nugent 1988 and Kalnajs cited in Saha et al. 1996). Indeed, structural and kinematic projection can be written as a convolution:

$$F(X) = \int_{-\infty}^{\infty} f(x)\,K(X-x)\,\mathrm{d}x\ ,$$

where $X=R^2$, $x=r^2$, $F(X)$ and $f(x)$ correspond to either $\Sigma(R)$ and $\rho(r)$ (structural projection) or $P(R)$ and $(1-\beta)\,p+\int_r^\infty \beta\,p\,\mathrm{d}s/s$ (anisotropic kinematic projection, following Wolf et al., which simplifies to p for isotropic kinematic projection), and where

$$K(y) = \begin{cases} (-y)^{-1/2} & y \leqslant 0\ , \\ 0 & y > 0\ . \end{cases}$$

Hence, with the convolution theorem, deprojection is obtained by applying an inverse Fourier transform to

$$\widetilde{f}(\omega) = \frac{1}{\sqrt{2\pi}}\,\frac{\widetilde{F}(\omega)}{\widetilde{K}(\omega)} = (1+i)\,\mathrm{sgn}(\omega)\,\sqrt{\frac{\omega}{2\pi}}\,\widetilde{F}(\omega) = [1+i\,\mathrm{sgn}(\omega)]\,\sqrt{\frac{|\omega|}{2\,\pi}}\,\widetilde{F}(\omega)\ ,$$

where $\widetilde{f}(\omega)$, $\widetilde{K}(\omega)$ and $\widetilde{F}(\omega)$ are the Fourier transforms of $f(x)$, $K(y)$ and $F\left(|X|\right)$, respectively (note the absolute values in the last term). A comparison of the accuracy of the two deprojection techniques is beyond the scope of the present article.

Our mass inversion algorithm should serve as a useful technique to get around the mass-anisotropy degeneracy in the case where the anisotropy profile is thought to be known. As mentioned in the end of Sect. I, there is a good convergence on the anisotropy profiles of ΛCDM halos as well as those of elliptical galaxies formed by binary mergers of spiral galaxies. Moreover, the anisotropy profile in many simulations appears linearly related to the slope of the (tracer) density profile (Hansen & Moore 2006), and this can be used to lift the mass-anisotropy degeneracy. A first application of our algorithm was given by Biviano & Salucci (2006) for the analysis of stacked clusters of galaxies.

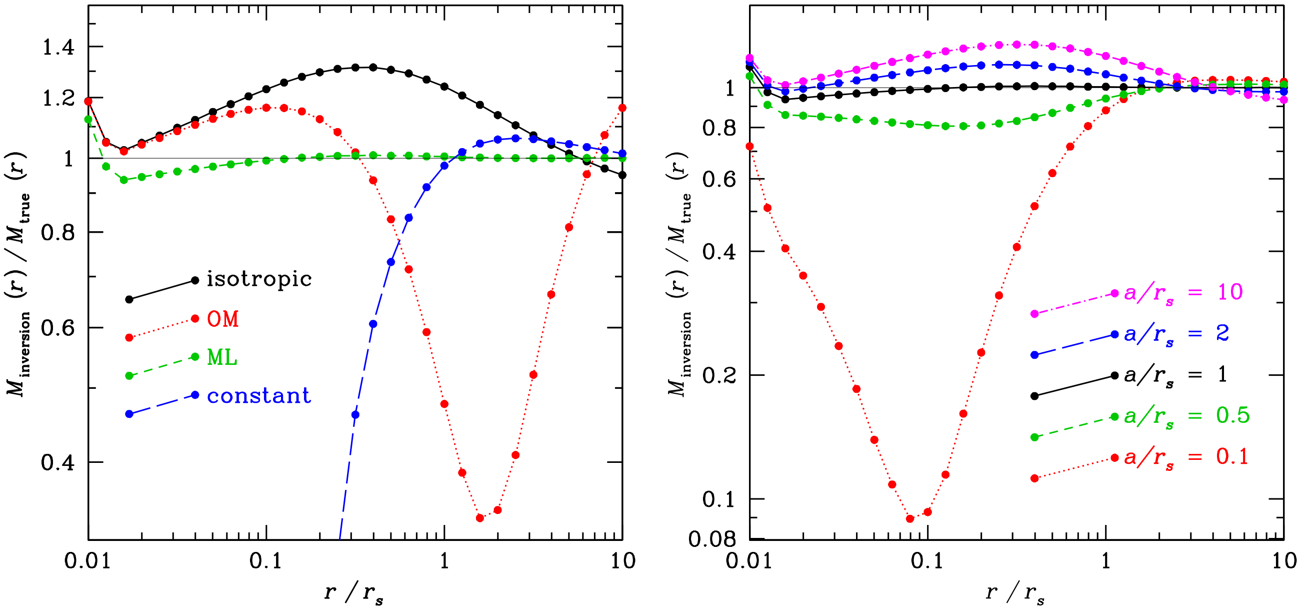

Figure 3. Robustness of the mass inversion to the wrong choice of anisotropy profile. *Left:* Same as right panel of Fig. 1, where the true anisotropy profile is now always an $a = r_s$ Mamon-Łokas model, but assuming that of the other three anisotropy models. *Right:* Same as left panel, but where the assumed anisotropy profile is always the $a = r_s$ Mamon-Łokas model, but with 5 different choices for a/r_s.

The mass inversion technique has the advantage of producing a non-parametric[10] mass profile, which can then be used to test the popular parametrizations of the mass profile (or alternatively of the density profile, the circular velocity profile or the density-slope profile).

In Sect. 3, we show that, for a mock NFW galaxy cluster with mildly increasing radial velocity anisotropy as seen in ΛCDM halos and with typical line-of-sight velocity dispersion profiles, measured with 50 velocities per radial bin, the mass inversion should be accurate to typically better than 70% relative errors at most radii and better than 20% for anisotropy models other than the Osipkov-Merritt one at $r > 8\,r_s$. The relatively high errors are a consequence of the double derivative of the observed projected pressure, $\mathrm{d}^2P/\mathrm{d}R^2$, that enters the mass inversion equation (68) or (69), through the term $p_{\rm iso}$, or in equation (82) or (83) for the special cases of anisotropy models. The errors are high at radii smaller than the first radial bin of the observed line-of-sight velocity dispersion profile. This illustrates the concept that kinematical modelling can only recover the mass and anisotropy at radii corresponding to the projected radii of the data. Nevertheless, with power-law extrapolations of the data to outer radii, we show that the mass inversion can recover mass profiles with good accuracy far beyond the outermost data point. Note that the mass inversion involves integrals out to infinity (e.g. eq. [83]), so one expects that the method should be most accurate when the tracer density profile falls fast at large radii. Our use of the NFW model for the tracer, with its shallow outer slope of $\mathrm{d}\ln\rho/\mathrm{d}\ln r = -3$ is thus expected to provide poorer results for the mass inversion than for steeper tracer density profiles.

We found that the recovered mass is correctly returned, independently of the shape of the anisotropy profile at $r = 7\,r_s$, and independently of the anisotropy radius for our chosen anisotropy model at $r = 3\,r_s$. A similar independence of the recovered mass on the assumed anisotropy profile has been recently noticed by Wolf et al. (2009) in the context of dwarf spheroidal and elliptical galaxies (for which the dark matter may not follow the stars, which themselves do not follow the NFW model). However, Wolf et al. prove analytically that this robustness to the anisotropy model occurs near the the radius of slope -3. Now, the NFW model has shallower slopes everywhere, reaching -3 at infinite radius. Wolf et al. notice that, for density profiles similar to those of ellipticals and dwarf spheroidals, the radius of slope -3 is close to the half-mass radius. In contrast, in the current context of clusters, the NFW model is divergent in mass (eq. [86]), and the concept of half-mass radius is ill-defined. Moreover, the radius where the mass is recovered for all anisotropy models tested is at 7 scale radii, which is outside the virial radius, hence not comparable to the half-light radius of elliptical and dwarf spheroidal galaxies. Fixing the anisotropy to the Mamon-Łokas model (which Mamon & Łokas 2005b found to be a good fit to the anisotropy profile of the halos in ΛCDM cosmological simulations), the recovered mass is most robust to the anisotropy radius at $3\,r_s$, which is roughly two-thirds of the cluster virial radius, again not directly comparable to the half-light radius of dwarf spheroidals and ellipticals.

The mass inversion technique is thus a useful complement to the set of tools one has to lift the mass-anisotropy degeneracy in spherical systems. Mass inversion is certainly not the privileged tool, but should be considered as one of many tools for the *exploratory data analysis* of spherical systems viewed in projection, in addition to anisotropy inversion, fitting models to the line-of-sight velocity dispersion and possibly kurtosis profiles, and fitting models, distribution functions, orbits and N-body systems to the distribution of particles in projected phase space. Ideally, one would analyze the kinematics of spherical systems using a variety of these tools. We are preparing such global analyses on dwarf spheroidal and elliptical galaxies, as well as on groups and clusters of galaxies.

---

[10] Although the algorithm uses a parametrized anisotropy profile and a smooth fit through the projected pressure profile, the mass profile that comes out is non-parametric.

ACKNOWLEDGMENTS

We thank Andrea Biviano for suggesting one of us (G.A.M.) to estimate $\rho\,\sigma_r^2$ given $\Sigma\,\sigma_{\rm los}^2$, i.e. to perform the kinematical deprojection, Joe Wolf for useful discussions during the final stage of this work (prompting us to return to this work after much neglect for over a year), as well as Aaron Romanowsky for useful comments. We are highly indebted to Richard Trilling for his critical reading of the manuscript, which helped us spot and fix several mathematical errors, and to the referee, Prasenjit Saha, for pointing out to us that projection is essentially a convolution and for his comments that improved the readability of the manuscript.

REFERENCES

Alard C., Colombi S., 2005, MNRAS, 359, 123
Ascasibar Y., Gottlöber S., 2008, MNRAS, 386, 2022
Bicknell G. V., Bruce T. E. G., Carter D., Killeen N. E. B., 1989, ApJ, 336, 639
Binney J., Mamon G. A., 1982, MNRAS, 200, 361
Biviano A., Salucci P., 2006, A&A, 452, 75
Blumenthal G. R., Faber S. M., Flores R., Primack J. R., 1986, ApJ, 301, 27
Cretton N., Emsellem E., 2004, MNRAS, 347, L31
de Lorenzi F., Debattista V. P., Gerhard O., Sambhus N., 2007, MNRAS, 376, 71
Dejonghe H., 1989, ApJ, 343, 113
Dejonghe H., Merritt D., 1992, ApJ, 391, 531
Dekel A., Stoehr F., Mamon G. A., Cox T. J., Novak G. S., Primack J. R., 2005, Nature, 437, 707, arXiv:astro-ph/0501622
Diemand J., Moore B., Stadel J., 2004, MNRAS, 352, 535
Emsellem E., Monnet G., Bacon R., 1994, A&A, 285, 723
Fukushige T., Makino J., 1997, ApJ, 477, L9
Gerhard O., Jeske G., Saglia R. P., Bender R., 1998, MNRAS, 295, 197
Gnedin O. Y., Kravtsov A. V., Klypin A. A., Nagai D., 2004, ApJ, 616, 16
Hansen S. H., Moore B., 2006, New Astronomy, 11, 333
Hansen S. H., Moore B., Zemp M., Stadel J., 2006, Journal of Cosmology and Astro-Particle Physics, 1, 14
Hénon M., 1982, A&A, 114, 211
Humphrey P. J., Buote D. A., Gastaldello F., Zappacosta L., Bullock J. S., Brighenti F., Mathews W. G., 2006, ApJ, 646, 899
Jing Y. P., Suto Y., 2002, ApJ, 574, 538
Kalal M., Nugent K. A., 1988, Appl. Opt., 27, 1956
Kazantzidis S., Magorrian J., Moore B., 2004, ApJ, 601, 37
Łokas E. L., 2002, MNRAS, 333, 697
Łokas E. L., Mamon G. A., 2003, MNRAS, 343, 401
Lupton R., 1993, Statistics in theory and practice. Princeton University Press, Princeton, NJ
Mamon G. A., Biviano A., Murante G., 2009, A&A, to be submitted
Mamon G. A., Łokas E. L., 2005a, MNRAS, 362, 95
—, 2005b, MNRAS, 363, 705
—, 2006, MNRAS, 370, 1582
Mamon G. A., Łokas E. L., Dekel A., Stoehr F., Cox T. J., 2006, in Mass Profiles and Shapes of Cosmological Structures, Mamon G. A., Combes F., Deffayet C., Fort B., eds., Ed. de Physique, Paris, pp. 139–148, arXiv:astro-ph/0601345
Merritt D., 1985, ApJ, 289, 18
Merritt D., Saha P., 1993, ApJ, 409, 75
Moore B., Quinn T., Governato F., Stadel J., Lake G., 1999, MNRAS, 310, 1147
Navarro J. F., Frenk C. S., White S. D. M., 1996, ApJ, 462, 563
Navarro J. F., Hayashi E., Power C., Jenkins A. R., Frenk C. S., White S. D. M., Springel V., Stadel J., Quinn T. R., 2004, MNRAS, 349, 1039
Osipkov L. P., 1979, Soviet Astronomy Letters, 5, 42
Prugniel P., Simien F., 1997, A&A, 321, 111
Richstone D., Gebhardt K., Aller M., Bender R., Bower G., Dressler A., Faber S. M., Filippenko A. V., Green R., Ho L. C., Kormendy J., Lauer T. R., Magorrian J., Pinkney J., Siopis C., Tremaine S., 2004, ApJ, submitted, arXiv:astro-ph/0403257
Richstone D. O., Tremaine S., 1984, ApJ, 286, 27
Romanowsky A. J., Strader J., Spitler L. R., Johnson R., Brodie J. P., Forbes D. A., Ponman T., 2009, AJ, 137, 4956
Saha P., Bicknell G. V., McGregor P. J., 1996, ApJ, 467, 636
Sanchis T., Łokas E. L., Mamon G. A., 2004, MNRAS, 347, 1198
Schwarzschild M., 1979, ApJ, 232, 236
Solanes J. M., Salvador-Solé E., 1990, A&A, 234, 93
Stoehr F., 2006, MNRAS, 365, 147
Stoehr F., White S. D. M., Tormen G., Springel V., 2002, MNRAS, 335, L84
Syer D., Tremaine S., 1996, MNRAS, 282, 223

Thomas J., Saglia R. P., Bender R., Thomas D., Gebhardt K., Magorrian J., Richstone D., 2004, MNRAS, 353, 391
Tiret O., Combes F., Angus G. W., Famaey B., Zhao H. S., 2007, A&A, 476, L1
Tonry J. L., 1983, ApJ, 266, 58
Tormen G., Bouchet F. R., White S. D. M., 1997, MNRAS, 286, 865
Tremaine S., Richstone D. O., Byun Y.-I., Dressler A., Faber S. M., Grillmair C., Kormendy J., Lauer T. R., 1994, AJ, 107, 634
Valluri M., Merritt D., Emsellem E., 2004, ApJ, 602, 66
Williams M. J., Bureau M., Cappellari M., 2009, MNRAS, in press, arXiv:0909.0680
Wojtak R., Łokas E. L., Gottlöber S., Mamon G. A., 2005, MNRAS, 361, L1
Wojtak R., Łokas E. L., Mamon G. A., Gottlöber S., Klypin A., Hoffman Y., 2008, MNRAS, 388, 815
Wolf J., Martinez G. D., Bullock J. S., Kaplinghat M., Geha M., Muñoz R., Simon J. D., Avedo F., 2009, MNRAS, submitted, arXiv:0908.2995

APPENDIX A: ABEL DEPROJECTION

In this appendix, we remind the reader of the derivation of the deprojection of equation (7) with the Abel inversion. Consider

$$J(r) = \int_r^\infty \frac{\Sigma(R)\,R\,\mathrm{d}R}{(R^2-r^2)^{1/2}} \ . \tag{A1}$$

Replacing $\Sigma(R)$ in equation (A1) by its definition in equation (7), one finds, after inverting the order of integration:

$$J(r) = 2\int_r^\infty \rho(s)\,s\,\mathrm{d}s \int_r^s \frac{R\,\mathrm{d}R}{(R^2-r^2)^{1/2}\,(s^2-R^2)^{1/2}} \ . \tag{A2}$$

The internal integral in equation (A2) is equal to $\pi/2$, as inferred from the substitution $\sin^2\theta = (R^2-r^2)/(s^2-r^2)$. Hence,

$$J(r) = \pi \int_r^\infty \rho(s)\,s\,\mathrm{d}s \ ,$$

and therefore

$$\rho(r) = -\frac{1}{\pi r}\frac{\mathrm{d}J}{\mathrm{d}r} \ . \tag{A3}$$

Now integrating equation (A1) by parts, one gets

$$J(r) = \lim_{R\to\infty} \sqrt{R^2-r^2}\,\Sigma(R) - \int_r^\infty \frac{\mathrm{d}\Sigma}{\mathrm{d}R}\left(R^2-r^2\right)^{1/2}\,\mathrm{d}R \ , \tag{A4}$$

For all realistic density profiles, $\Sigma(R)$ falls faster than R^{-1}, as is the case for the surface density profiles of globular clusters, elliptical galaxies and clusters of galaxies. Hence, the surface term in equation (A4) is zero and one can write

$$\frac{\mathrm{d}J}{\mathrm{d}r} = r\int_r^\infty \frac{\mathrm{d}\Sigma}{\mathrm{d}R}\frac{\mathrm{d}R}{(R^2-r^2)^{1/2}} \ . \tag{A5}$$

Inserting the derivative of J of equation (A5) into equation (A3) leads to equation (8). The surface term that survived when $\Sigma \propto 1/R$ disappears in the derivative.

APPENDIX B: KINEMATIC DEPROJECTION FOR THE TANGENTIAL DYNAMICAL PRESSURE

In this appendix, we derive equations (31) and (32) for the tangential dynamical pressure.

Differentiating equation (23), one finds to get the differential equation

$$p'_\theta - \frac{\beta}{1-\beta}\frac{p_\theta}{r} = p'_{\rm iso} \ . \tag{B1}$$

Now, if we write

$$p'_\theta - \frac{\beta}{1-\beta}\frac{p_\theta}{r} = \frac{1}{f}\frac{\mathrm{d}(f p_\theta)}{\mathrm{d}r} \ , \tag{B2}$$

then equations (B1) and (B2) lead to

$$p_\theta(r) = -\frac{1}{C_\beta(r)}\int_r^\infty f\,p'_{\rm iso}\,\mathrm{d}s \ , \tag{B3}$$

where the upper limit at infinity ensures that $p_\theta = (1-\beta)\,\rho\,\sigma_r^2$ does not reach negative values at a finite radial distance. But equation (B2) directly gives

$$\frac{\mathrm{d}\ln f}{\mathrm{d}\ln r} = -\frac{\beta(r)}{1-\beta(r)} \, ,$$

hence

$$g(r) = g(r_1)\, \exp\left(-\int_{r_1}^{r} \frac{\beta}{1-\beta}\,\frac{\mathrm{d}s}{s}\right) \tag{B4}$$

for any arbitrary r_1. With equation (B4), equation (B3) allows one to recover equation (31):

$$\begin{aligned} p_\theta(r) &= -\exp\left(\int_{r_1}^{r} \frac{\beta}{1-\beta}\,\frac{\mathrm{d}s}{s}\right)\int_r^\infty \exp\left(-\int_{r_1}^{s} \frac{\beta}{1-\beta}\,\frac{\mathrm{d}t}{t}\right) p'_{\rm iso}\,\mathrm{d}s \, , \\ &= -\int_r^\infty \exp\left(-\int_{r}^{s} \frac{\beta}{1-\beta}\,\frac{\mathrm{d}t}{t}\right) p'_{\rm iso}\,\mathrm{d}s \, , \end{aligned} \tag{B5}$$

where the second equality is obtained adopting $r_1 = r$.

Integrating by parts the integral in equation (B5), we finally recover equation (32)

$$p_\theta(r) = p_{\rm iso}(r) - \int_r^\infty p_{\rm iso}\frac{\beta}{1-\beta}\,\exp\left(-\int_r^s \frac{\beta}{1-\beta}\,\frac{\mathrm{d}t}{t}\right)\frac{\mathrm{d}s}{s} \, .$$